

Atoms of Thought: Universal EEG Representation Learning with Microstates

Xinyang Tian*

Institute for Interdisciplinary
Information Sciences, Tsinghua
University
Beijing, China
xinyangtian368@gmail.com

Ruitao Liu*

Institute for Interdisciplinary
Information Sciences, Tsinghua
University
Beijing, China
liurt23@mails.tsinghua.edu.cn

Ziyi Ye[†]

Institute of Trustworthy Embodied AI,
Fudan University
Shanghai, China
zyye@fudan.edu.cn

Siyang Xue

School of Clinical Medicine, Tsinghua
University
Beijing, China
xuesy22@mails.tsinghua.edu.cn

Xin Wang

Beijing Five Seasons Medical
Technology Co., Ltd.
Beijing, China
www.wangshin15@gmail.com

Xuesong Chen[‡]

Beijing Five Seasons Medical
Technology Co., Ltd.
Beijing, China
chenxuesong1128@163.com

Abstract

Learning universal representations from electroencephalogram (EEG) signals is a cutting-edge approach in the field of neuroinformatics and brain-computer interfaces (BCIs). Conventionally, EEG is treated as a multivariate temporal signal, where time- or frequency-domain features are extracted for representation learning. This paper investigates a simple yet effective EEG representation, i.e., microstates. Microstates represent the building blocks of brain activity patterns at a microscopic time scale. We build a universal microstate tokenizer from a large medical EEG dataset by clustering continuous EEG signals into sequences of discrete microstates. The microstate tokenizer is then adopted universally across a series of downstream tasks, including sleep staging, emotion recognition, and motor imagery classification. Experimental results show that EEG representation learning with microstates outperforms traditional time-domain and frequency-domain features under different models and across different tasks. Further analysis shows that microstates offer greater interpretability and scalability, thereby opening up applications in both cognitive neuroscience and clinical research.

Keywords

EEG Analysis, Microstates, Sleep Staging, Emotion Recognition, Motor Imagery Classification

Accepted by the 3rd International Workshop on Multimodal and Responsible Affective Computing (MRAC 2025). Version of Record DOI: 10.1145/3746270.3760230.

1 Introduction

Electroencephalogram (EEG) signals provide valuable insights into brain activity, making them indispensable in fields such as clinical medicine, neuroscience, and cognitive psychology [80]. For example, EEG has been widely used in clinical settings to detect certain diseases and anomalies [9, 38, 59], to investigate neural

mechanisms underlying cognitive processes [40, 56], and to design brain-computer interfaces [26]. Recently, with the maturity of deep learning techniques, integrating AI technology with EEG analysis has become the new paradigm, significantly improving classification performance in downstream tasks [1, 3].

Despite these merits, EEG signals are highly non-linear and non-stationary [62], which pose challenges to extracting effective representations from EEG signals. Conventionally, EEG is treated as multivariate time series data with features extracted in the time and frequency domain for further analysis [62]. Such features come with two major drawbacks. On the one hand, they **are susceptible to artifacts and are prone to be confined within a task-specific and subject-specific representation space**. Conventional time and frequency domain EEG representations will inevitably incorporate artifacts [58] related to eye blinks, myoelectricity, and the environment. Additionally, time and frequency domain EEG representations vary significantly across subjects and tasks, making it challenging to generalize. This results in suboptimal performance on a single task and degraded generalizability across different tasks [29], and requires huge amounts of task-specific data, which are usually unavailable. On the other hand, time- and frequency-domain features are **unable to uncover transient and dynamic information**. Conventional methods often struggle to capture high-resolution EEG features. Time-domain information, which directly utilizes raw EEG signals, is often considered inefficient due to its low signal-to-noise ratio (SNR) [67]. Frequency-domain information uses a fixed window length, which consequently obscures temporal resolution and results in a certain degree of information loss [14, 62].

To address these challenges, we introduce a novel approach that integrates deep learning with a biologically grounded concept in EEG analysis: EEG microstates [35]. EEG microstates are quasi-stable discrete patterns of scalp electrical potential that last for brief periods, typically 60-120 milliseconds [43]. While conventional features tend to ignore the physiological and clinical context of EEG signals, EEG microstates are believed to correspond to fundamental and stable cognitive states [20, 43, 76]. Previous researchers have revealed a series of underlying mechanisms of thought and cognition [10, 36, 44, 56]. Building on such results, we leverage EEG

*Both authors contributed equally to this research.

[†]Research was conducted as a Ph.D. student at Tsinghua University.

[‡]Corresponding author. Email: chenxuesong1128@163.com

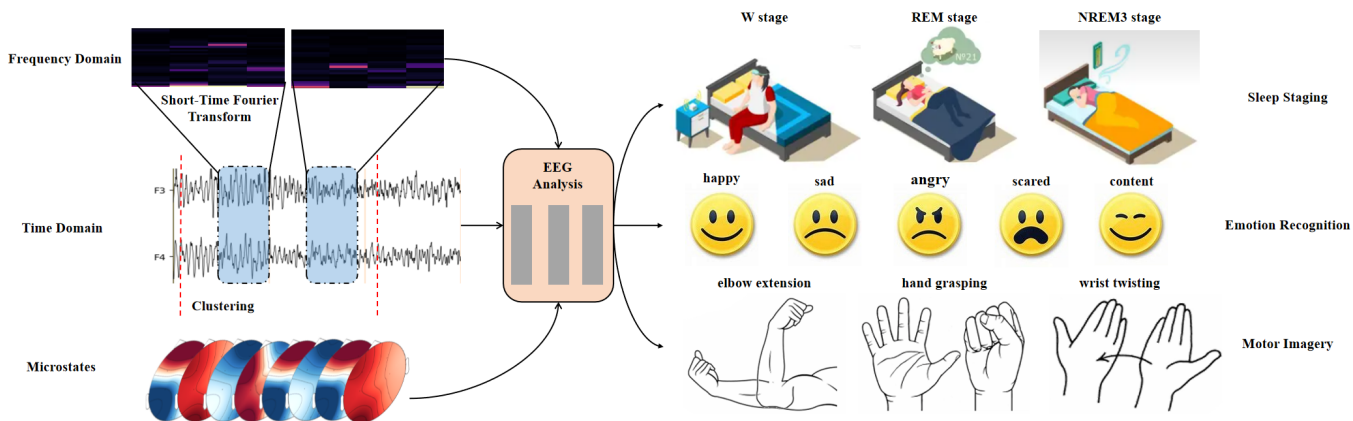


Figure 1: Visualization of Different Representations and Downstream Tasks. Conventional representations mainly reside in the time domain and frequency domain. We propose the microstate representation, which is a universal representation that outperforms other representations under different model structures and across different tasks [8, 15, 34].

microstates as a discrete and intrinsic representation of brain activity that is more aligned with the underlying neural mechanisms, improving both interpretability and robustness. We validate the effectiveness of EEG microstates across three critical tasks—sleep staging, emotion recognition, and motor imagery [6, 80] and with different models, showing superior performance compared to conventional representations. Moreover, we test the accuracy of EEG representation learning with increasing data size, observing that EEG microstates show greater performance gain than conventional features. Furthermore, we investigate the distribution of EEG microstates across various cognitive functions and present a potential relationship to interpret cognitive functions with EEG microstates.

The main contributions of this work are as follows:

- We introduce EEG microstates as a universal representation of brain activity, bridging the gap between deep learning techniques and neural activity patterns.
- We demonstrate the effectiveness of this microstate-based approach in three critical tasks—sleep staging, emotion recognition, and motor imagery classification, and with different model structures. Experimental results indicate that the microstate tokenizer initialized in one task can be generalized to a series of downstream tasks, showcasing its universal applicability and alleviating the impact of data scarcity.
- We conduct in-depth analysis showing that EEG microstate is more scalable than time-domain and frequency-domain methods and can serve as an explainable feature linking to various cognitive functions.

2 Related Work

EEG analysis has long been a critical tool in both clinical diagnosis and research, with various representation learning methods to enhance the accuracy of diagnosis. This section elaborates on a variety of techniques developed to extract meaningful information from the brain’s electrical activity, particularly in the medical and deep learning fields.

2.1 EEG Microstates in Cognitive Neuroscience

EEG microstate analysis was first introduced by Lehmann et al. [35], and has gained significant attention as a promising tool for representing brief, stable patterns of brain activity. Microstates are thought to reflect fundamental cognitive states that the brain switches between, providing valuable insights into the temporal organization of brain function [43]. Studies have shown that various diseases, such as epilepsy, sleep disorder and Alzheimer’s disease, can alter EEG microstates [11, 23, 33, 39, 52, 63]. Recent research has applied microstate analysis to a wide range of cognitive tasks, including emotion, attention, and social abilities [22, 24, 51, 54, 55], demonstrating the effectiveness of microstates in understanding cognitive and pathological states.

The most common approach to producing microstates originates from Pascual-Marqui et al. [47]. They used the k-means clustering method to conduct the EEG microstate analysis, which further become the most popular technique for microstate classification. Other studies have introduced alternative methods for microstate analysis, which are based on a series of clustering algorithms [28, 41, 42, 45, 50].

However, most existing research has focused on interpreting microstates based on the physical conditions of subjects, while efforts to learn EEG representations for downstream classification and detection tasks remain limited. Moreover, the interpretability of microstates and their connection to fundamental cognitive states make them a promising candidate for representing EEG signals in contemporary deep-learning models, yet no current studies have tested this potential.

2.2 Representation Learning for EEG Analysis

Machine learning, especially deep learning techniques have been increasingly integrated into EEG analysis to improve the accuracy and efficiency of EEG-based classification tasks. Typically, machine learning models require EEG representations extracted from the raw signals as input, which can be broadly categorized into time- and frequency-domain features. On the one hand, raw EEG itself

can serve as the most straightforward time-domain representation. Al-Hussaini et al. [5] used fixed-length windows of 30s segmented from raw EEG signals during prototype learning for sleep staging, which treated the signals as multivariate time series data. Perslev et al. [48] also used raw EEG signals as their CNN-based model representation for sleep staging.

On the other hand, information in the frequency domain is also commonly extracted as EEG representations. V. and Bhattacharyya [64] used multivariate variational mode decomposition (MVMD) to extract spectral information for emotion recognition. Zheng et al. [78] used the Hilbert-Huang transform to analyze scalp EEG signals. It has been shown in [71, 81] that using frequency-domain information improves performance in emotion recognition.

Despite the above achievements brought about by deep learning, conventional representations often contain person- or task-specific artifacts [60, 70, 72]. Due to the models' susceptibility to noise and artifacts, training such models either undermines their performance and generalizability, or requires a huge amount of person- or task-specific data.

To address these challenges, Afzal et al. [1] proposed a novel graphical representation of raw EEG data, which improves seizure detection but is still task-specific. Based on the development of time-domain representations and suitable model structures [17, 46, 74] and inspired by the development in natural language processing (NLP), Gui et al. [27] proposed a vector quantization pre-training method to obtain representations for downstream tasks. Wang et al. [69] also utilized a pre-training paradigm to extract relevant representations by spatio-temporal representation alignment in order to depict the brain. They observed that such representations can be better generalized across downstream tasks, but consume a large amount of computational power and time. Moreover, the input EEG signal of the pre-trained model is still treated as multivariate time series data.

3 EEG Representations

This section lists conventional EEG representations in the time-domain and frequency-domain, and our microstate representation. It also elaborates on detailed methods and procedures to construct different representations.

3.1 Problem formulation

The objective of EEG signal analysis and physical state prediction can be defined as follows: We are given the input raw EEG signal $s \in \mathbb{R}^{C \times f_s T}$ where C denotes the number of channels, f_s is the sampling frequency and T is the sample duration. The EEG signal analysis aims to predict the physical state of the sampled subject, which can be represented by a sequence of discrete labels $l = L^{f_i T}$ where $L = \{a_1, a_2, \dots, a_m\}$ is the set of labels and f_i is the state frequency.

3.2 Time-Domain Features Extraction

The most straightforward approach for EEG analysis is to directly utilize the time-domain information features, i.e., the raw EEG signals [62]. In this setting, the raw EEG signal is sliced into fixed-length windows with duration T_w , and the feature $s_{time,w}$ will be of the shape of $\mathbb{R}^{C \times f_s T_w}$, with the corresponding labels $l_w \in L^{f_i T_w}$.

3.3 Frequency-Domain Features Extraction

Raw EEG signals often obscure frequency information, and thus, sometimes directly using it does not produce desirable results. Therefore, a common approach to handling such time-domain signals is to use their corresponding frequency-domain signals as features [65].

Frequency Bands. The frequency-domain representations are extracted based on the frequency power distribution among frequency bands [75]. The frequency domain are divided into several frequency bands, including the δ -band (0.5 ~ 4Hz), θ -band (4 ~ 8Hz), α -band (8 ~ 12Hz), σ -band (12 ~ 16Hz), β -band (16 ~ 30Hz) and γ -band (30 ~ 40Hz).

Short-Time Fourier Transform (STFT). Time-frequency transformation can be carried out via numerous methods, namely short-time Fourier transform (STFT), discrete/continuous wavelet transform (DWT/CWT), and empirical mode decomposition (EMD) [4, 32]. Short-time Fourier transform, owing to its straightforwardness and thorough theoretical analysis, is applied in many EEG-related tasks [12, 18, 30, 68]. Consequently, we choose this method as our frequency-domain baseline.

Given the raw EEG signal of a single measurement channel $s_{sin} \in \mathbb{R}^{f_s T}$, we perform short-time Fourier transform with fixed window size t_w and overlap ratio r_o . The length after the short-time Fourier transform will be

$$l_{freq} = \left\lceil \frac{f_s T - f_s t_w}{(1 - r_o) f_s t_w} \right\rceil + 1$$

and if we leave out the margin then the resulting length will be

$$l_{freq} = \frac{f_s T}{(1 - r_o) f_s t_w} = f_{freq} T$$

$$f_{freq} = \frac{1}{(1 - r_o) t_w}$$

Using STFT, we obtain a frequency axis F_a and time axis T_a and the amplitude of the signal at each frequency $f \in F_a$ and time point $t \in T_a$. Note that $|T_a| = l'$ and hence the output shape is $s_{f,t,sin} \in \mathbb{R}^{|F_a| \times l'}$.

Band Power Integration. Now that we have obtained the single channel data $s_{freq,sin} \in \mathbb{R}^{F \times l_{freq} T}$ where F is the frequency resolution, we integrate the rows that correspond to each frequency band to obtain the total power within that band. In this case, the integration result will have shape $\mathbb{R}^{B \times l_{freq} T}$. By flattening and stacking all channels, the final result has shape $s_{freq} \in \mathbb{R}^{N \times B l_{freq} T}$.

3.4 Unsupervised Microstate Tokenizer

Our clustering method is based on k-means [47]. But to guarantee that the clustering model has a sufficient level of generalizability, unlike previous works, we have to fit the clustering model on a huge amount of data. To allow the model to take all data points into consideration without consuming too much memory, we use incremental learning by dividing data into small batches of size n .

3.4.1 Stream Clustering [2]. The original k-means algorithm clusters the data points by initially selecting k centers, grouping data points according to their distance to the centers, and computing

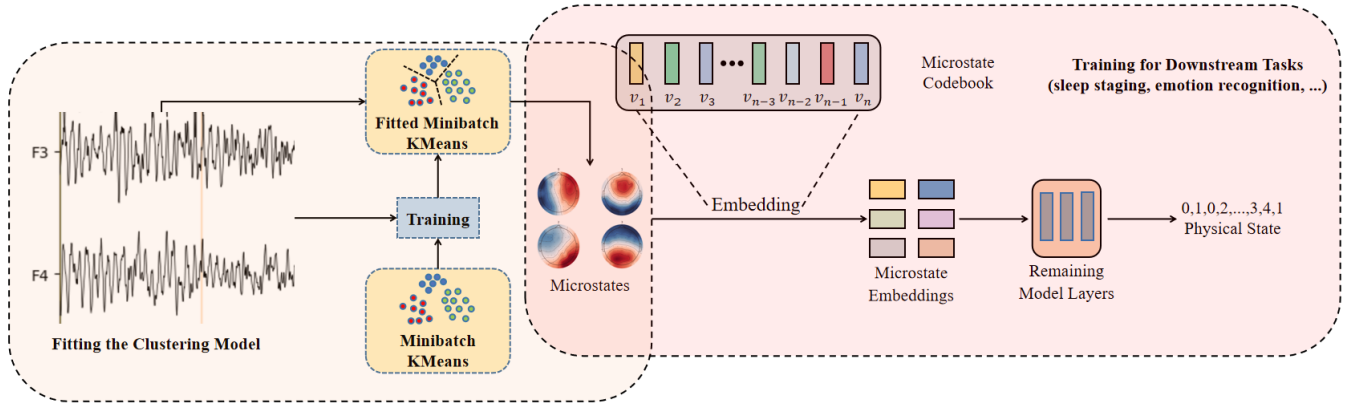


Figure 2: Pipeline of our Work. Our work can be broken into two parts. The first involves fitting a tokenizer to extract microstates from six EEG channels F3, F4, C3, C4, O1, O2. The second consists of training different models on the microstate signals and performing downstream tasks. The tokenizer of the first stage is independent of the models of the second stage. For each task, the model always includes an embedding layer to convert the discrete microstates into high-dimensional embeddings [8].

the centroid of each cluster as the new centers. The algorithm terminates when reaching the maximum iterations or the positions of the centers have converged.

Streaming k-means follows a fashion similar to classical k-means, but each time it uses only a small batch of data to update the cluster centers. Therefore, we do not need to store the entire dataset in memory, while only need to store a batch. This renders better performance than using only a small portion of data, and reduces memory consumption compared to clustering on all data points. The procedure is shown in Algorithm 1.

Algorithm 1 Streaming K-Means

```

Initialize cluster centers  $c_1, c_2, \dots, c_k \in \mathbb{R}^C$ 
 $iter \leftarrow 0$ 
while  $iter < max\_iter$  and centers have not converged do
  Get a new batch  $d_1, d_2, \dots, d_n \in \mathbb{R}^C$ 
   $S_i \leftarrow \{d_j | \arg \min_r \|d_j - c_r\|^2 = i\}$ 
   $c_i \leftarrow \frac{1}{|S_i|} \sum_{r=1}^{|S_i|} S_{ir}$ 
end while

```

3.4.2 *Fitting the Clustering Model.* We adopt the following experimental setup.

Dataset. We select the **Human Sleep Project (HSP)** dataset to fit the clustering model [73]. The dataset includes polysomnography (PSG) data from over 20K subjects and is still growing in size. The reasons why we use EEG data recorded during sleep are as follows:

- It is usually difficult and costly to record EEG signals during wakefulness, and these datasets are usually limited in size
- Currently the community has abundant sleep data. They can also reflect the cognitive level and consciousness, despite the fact that their being less organized, noisy and has a limited number of channels (usually 6 channels)

- We want to test whether we can model brain activity during sleep data, which can be generalized to downstream tasks during wakefulness

Extracting target channels. Since PSG signal involves numerous components like EEG, EOG, and ECG, the number of channels comes with varying sizes due to loss of data or shortage of equipment. Consequently, we filter out all channels except N of them that are present in all samples. The generic method will be clustering the data by treating them as N dimensional points. In the HSP dataset, only the channels F3, F4, C3, C4, O1, O2 are present across a relatively large amount of subjects, whereas other channels only appears sporadically among very limited number of subjects. Consequently these 6 leads are selected for clustering, since we have to extract a generalizable representation across subjects in order to obtain a truly universal representation. After extracting the necessary channels from the original data $s \in \mathbb{R}^{C \times f_s T}$ we obtain the filtered data $s_{ext} \in \mathbb{R}^{N \times f_s T}$ where $N = 6$.

Filtering. A bandpass filter with low pass 1Hz and high pass 40Hz is applied to retain the most relevant frequency bands (e.g., delta, theta, alpha, beta). The array shape remains unchanged during this operation.

Resampling. The HSP dataset comes with different sample frequencies, including 256Hz and 512Hz. We resample the signals to 100Hz for better clustering results. Now the data shape becomes $s_{res} \in \mathbb{R}^{N \times f_{res} T}$ with $f_{res} = 100\text{Hz}$.

Global field power (GFP) peaks extraction. Global field power is computed as the standard deviation of all sensors. The peaks are defined as their local maxima, which have the highest signal-to-noise ratio [43]. Therefore, we extract GFP peaks on the six channels. This produces the final input for the clustering model, which has size $s_{gfp} \in \mathbb{R}^{N \times t}$ where t denotes the number of GFP peaks in the sequence $\mathbb{R}^{N \times f_{res} T}$.

Table 1: Classification accuracies and model parameters for sleep staging under different representations and different model architectures on the Human Sleep Project (HSP) dataset. The highest performance among all representations under a certain model is highlighted in boldface.

REPRESENTATION	CNN+LSTM			SLEEP TRANSFORMER			SLEEP NET ZERO		
	ACC	KAPPA	PARAMS	ACC	KAPPA	PARAMS	ACC	KAPPA	PARAMS
RAW EEG (TIME DOMAIN)	0.710	0.597	707K	0.786	0.702	3.2M	0.793	0.713	10.9M ¹
STFT (FREQUENCY DOMAIN)	0.778	0.690	692K	0.790	0.710	3.2M	0.794	0.711	3.2M
MICROSTATES (OURS)	0.801	0.722	687K	0.810	0.736	3.4M	0.810	0.736	3.2M

Fitting the clustering model. After obtaining the data of shape $s_{gfp} \in \mathbb{R}^{N \times t}$, we set the number of clusters $k = 1000$ and $n = 50$ for batch size and fit the GFP peaks.

3.4.3 Constructing the Microstates. Having fitted clustering model, we can apply it to raw EEG signals of shape $s \in \mathbb{R}^{N \times f_s T}$ to obtain the microstate sequence $c \in S^{f_s T}$, $S \in \{b_1, b_2, \dots, b_k\}$ with $k = 1000$. S is the set of microstates.

4 Downstream Tasks

In this section, we introduce the experimental setup for testing the performance of our microstate representation and conventional representations. The microstate sequence is produced by the tokenizer trained in the previous section (the fitted KMeans in Figure 2).

4.1 Sleep Staging

During different sleep stages, brain activity varies accordingly. This lies the foundation for predicting sleep stages using EEG signals.

Dataset. For sleep staging, we use the HSP dataset [73] mentioned in *fitting the clustering model* to test the performance of our representation.

Sleep stages. For sleep staging, L consists of the five sleep stages: {W, N1, N2, N3, R}. W corresponds to wake stage, N1, N2 and N3 correspond to different non-rapid eye movement (NREM) stages, and R corresponds to rapid eye movement (REM) stage.

Preprocessing. The EEG signal is filtered and resampled to $f_{res} = 100\text{Hz}$. For extracting frequency-domain information, we choose $t_w = 1\text{s}$ and $r_o = 0$. Finally, the EEG signal is sliced into $T_w = 300\text{s}$ windows.

Model Architecture. To test the universality of our microstate representation, we adopt the following model structures:

CNN+LSTM.[57] This model architecture consists of 3 CNNs and 2 GRUs for extracting spatial and temporal information, and fully connected layers for classification. An embedding layer is added for our microstate representation.

Sleep Transformer.[49] Sleep Transformer uses 2 Roformer [61] layers to extract the local and global features before inputting into the final linear layer. An embedding layer and 2 CNNs are added for our microstate representation.

Sleep Net Zero.[37] The model consists of a feature extraction unit composed of several residual blocks, a Roformer layer and a linear layer. To adapt to our microstate representation, we add an embedding layer and 4 CNNs, and remove the feature extraction unit.

Table 2: Classification accuracies and model parameters for emotion recognition (CNN-based model, SEED dataset) under different representations. The highest performance among all representations is highlighted in boldface.

REPRESENTATION	ACCURACY	KAPPA	PARAMS
RAW EEG (TIME DOMAIN)	0.846	0.769	19.1M
STFT (FREQUENCY DOMAIN)	0.797	0.694	19.1M
MICROSTATES (OURS)	0.862	0.793	20.1M

For time- and frequency-domain signals, we change the embedding layer into a convolution layer which functions similarly as the embedding.

Loss Function. The loss function is set as cross-entropy loss. Suppose that the output of the fully connected layer is $(h_1, h_2, h_3, h_4, h_5)$, which are the scores of the five classes. We perform a softmax on the scores and the cross entropy loss is defined as follows:

$$\text{loss} = - \sum_{i=1}^5 p(i) \log \text{Softmax}(h_i)$$

which is minimized when the correct label j has score h_j significantly larger than the other labels.

4.2 Emotion Recognition

Emotions are a key part of our physical state, and have a strong connection with brain activity. Consequently, our work involves training a microstate-based model for emotion classification.

Dataset. We use the SEED dataset [19, 79] for emotion recognition. The SEED dataset consists of 15 subjects watching video clips that express different emotions. The overall tone is categorized as positive, negative, and neutral. The EEG signal is recorded with 62 channels and at a frequency 200Hz.

Emotion Labels. We utilize the overall tone of each movie clip as our labels, and thus L consists of positive, negative, and neutral.

Preprocessing. We directly use the sample frequency $f_s = 200\text{Hz}$. We pad all samples to $T_w = 265\text{s}$. Other configurations are the same as in sleep staging.

Model Architecture. The model used here is a CNN-based classifier [31] with similar modifications and cross-entropy loss. It has 5 CNNs and 4 linear layers.

Table 3: Classification accuracies, model parameters for motor imagery classification (ResNet, Motor Movement/Imagery dataset) under different representations. The highest performance among all representations is highlighted in boldface.

REPRESENTATION	ACCURACY	KAPPA	PARAMS
RAW EEG (TIME DOMAIN)	0.362	0.149	20.3M
STFT (FREQUENCY DOMAIN)	0.323	0.097	21.5M
MICROSTATES (OURS)	0.437	0.250	21.4M

4.3 Motor Imagery Classification

Physical movement or imagination is another important factor of human physical status. Therefore our work involves predicting the movement or imagination activity via microstate sequences.

Dataset. We use the **Motor Movement/Imagery Dataset** [25, 53] for the task of motor imagery classification. The dataset consists of EEG signals sampled from 109 subjects. Each subject underwent 14 trials involving four tasks and two baseline rest sessions. The tasks are as follows:

- Task 1: Open and close the left or right fist.
- Task 2: Imagine opening and closing the left or right fist.
- Task 3: Open and close both fists or both feet.
- Task 4: Imagine opening and closing both fists or feet.

Movement/Imagery Labels. In this setting, we focus on the onset of movement/imagery and the labels L consists of left hand, right hand, both hands and both feet.

Preprocessing. In this dataset, each label corresponds to roughly 4s of EEG signals, and hence we choose $T_w = 4s$. Other configurations are the same as the above experiments.

Model Architecture. The model architecture is based on [13], which consists of a CNN and 3 residual blocks followed by 4 linear layers. We use configurations similar to the above.

5 Results and Analysis

We compared our proposed representation with conventional time- and frequency-domain representations across different tasks and under different model configurations.

5.1 Evaluation Metrics

We evaluated our representation with different model structures and across different tasks. The evaluation metrics are the classification accuracy and Cohen’s Kappa.

5.2 Microstates as a Universal Representation

We compared the accuracy and Cohen’s Kappa on the test set under 3 different models and across three key tasks with different representations. Results on sleep staging are shown in Table 1, and results on emotion recognition and motor imagery classification are shown in Table 2 and Table 3, respectively.

¹For Sleep Net Zero, more parameters are used since the input size of raw EEG signals is (6, 30000) which is six times that of microstates (30000, 6) and 17 times that of frequency-domain signals (6, 1800).

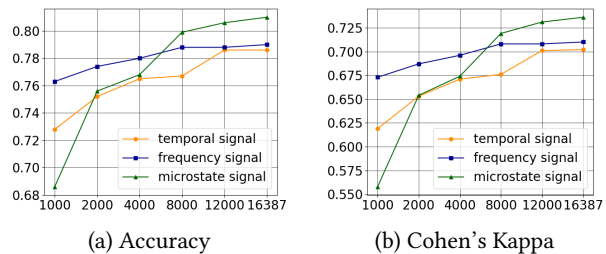


Figure 3: Accuracy (left) and Cohen’s Kappa (right) with different representations under Sleep Transformer and different number of samples.

Table 4: Classification accuracies and model parameters for emotion recognition (CNN-based model, SEED dataset) including full channels (62 in total). The highest performance among all representations is highlighted in boldface.

REPRESENTATION	ACCURACY	KAPPA	PARAMS
RAW EEG (6 CHANNELS)	0.846	0.769	19.1M
RAW EEG (62 CHANNELS)	0.854	0.778	19.2M
STFT (6 CHANNELS)	0.797	0.694	19.1M
STFT (62 CHANNELS)	0.854	0.778	19.1M
MICROSTATES (OURS)	0.862	0.793	20.1M

From Table 1, we observe that EEG representation with microstates outperforms time domain and frequency features in three different backbone models, including CNN+LSTM, Sleep Transformer, and Sleep Net Zero. Among the results, microstates achieve the highest accuracy of 0.81 using a sleep transformer or sleep net zero. This indicates that EEG microstates have the potential to serve as a universal representation and outperform temporal- and frequency-domain features across tasks and model structures. Similar observations are obtained in the emotion recognition task based on a CNN-based model and on the motor imagery classification task based on a ResNet model.

We also record the standard deviation of the performance of microstate representation on Sleep-Net-Zero, which gives an accuracy of $0.808(\pm 1.897 \cdot 10^{-3})$ and Kappa $0.733(\pm 2.482 \cdot 10^{-3})$.

We further compare the performance of time- and frequency-domain features with microstates. We see that frequency-domain representation performs well on sleep staging, while producing suboptimal results on other tasks. We suspect that this is because sleep staging is highly frequency-associated, while on other tasks, frequency-domain features may be weak due to information loss [14, 62] in raw EEG signals. On the other hand, raw EEG signals are often subject to noise [67] and does not produce optimal results. Compared to time- and frequency-domain features, microstates present a robust performance across datasets and classification models. This demonstrates that the microstate representation obtained from sleep EEG data can be generalized to various critical tasks and different models, serving as a universal representation.

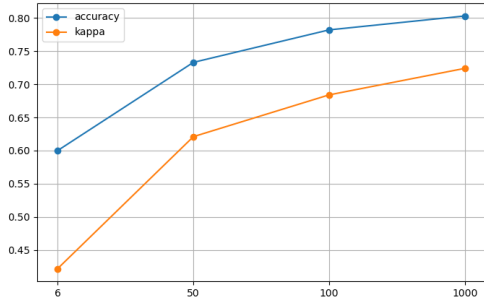


Figure 4: Accuracy and Cohen’s Kappa under Sleep Net Zero with different number of microstates.

5.3 Results using Full Channel Data

Due to data constraint, the microstate tokenizer is trained on data from only 6 channels. To allow for a comprehensive comparison, we test the performance of the CNN classifier on the SEED dataset using full channels (62 channels in total). The results are shown in Table 4.

From the results we see that using EEG signals from the 6 channels can achieve similar results to that of using full data, as is seen from the raw EEG signals that increasing the number of channels does not significantly boost performance. Notice that the performance of frequency-domain representation increases significantly, which we conjecture that it is because the additional channels compensate for the information loss during the time-frequency transformation. Results show that using only 6 channels does not significantly degrade performance, which justifies our clustering on these channels.

5.4 Microstates as a Scalable Representation

We further test the performance of EEG representation learning with microstates across different scales of training data in the sleep staging task under Sleep Transformer on the HSP dataset. We also find that microstates offer a more scalable representation. As shown in Figure 3, microstates do not exhibit strengthened performance when the size of the training data is smaller than 2,000. However, when the number of samples increases, the performance of the microstate representation shows a more pronounced performance gain in comparison to other features. Our experiment demonstrates that the microstate representation is also capable of scaling across the size of the training data. This reveals the potential of EEG representation with microstates, especially using deep learning methods and increased data size.

On the other side, we tested the performance of our tokenizer under different number of clusters by selecting different parameters k for clustering. We evaluated the model performance on the validation set with different number of microstates. The results are shown in Table 4. From the results we see that the performance increases while the number of microstates increases. Results show that the performance of the microstate representation also scales with increasing number of microstates.

5.5 Interpreting Microstates

In this section, we give an analysis of the interpretability of the microstate representation, which in turn leads to its better performance over other representations.

As mentioned in [58], one challenge in analyzing EEG signals is that they are highly subject-dependent and vary significantly across different people. Consequently, it is hard to extract effective inter-subject representations using conventional time- or frequency-domain information. Microstates solve this issue by providing a coarse-grained discrete representation that groups similar EEG states together. Its clustering-based nature guarantees its capability to extract universal features while retaining the differences.

We analyze the proportion of the most 20 frequently-occurring microstates among groups of 30 subjects under W, N3, and R stage. Results in Figure 5 show that under the same sleep stages, the most frequent microstates are common across all subject groups. For example, the microstates 419, 421, 385, 333 occur with high frequency among all subject groups during W and R stage, whereas the microstates 487, 378, 452, 651 occur with high frequency among all groups under N3 stage. This suggests that the microstate representation captures the similarity between subjects, albeit their having different EEG voltages. Hence this in turn prevents the model from being distracted towards personal specific nuances.

Furthermore, the most frequent microstates under W and R stages both contain 419 and 161. The state 419 has all its channels below $2.2\mu\text{V}$, denoting a state with a weak EEG signal, while the state 161 has its voltage within the interval $4 \sim 11\mu\text{V}$, which is also relatively low. This is consistent with the fact that during W stage, the EEG signal is dominated by α waves, which have a low amplitude and high frequency. Also, during R stage, the brain activity is similar to W stage since this is when dreams take place [21]. Consequently, it does not come as a surprise that W and R stages share many microstates in common, indicating a similar brain activity pattern. However, the microstate 378 denotes signals within the interval $10 \sim 24\mu\text{V}$, and 452 has signals within $-5 \sim -21\mu\text{V}$. Both of them are relatively strong brain activity. This is again consistent with the fact that during N3 the EEG signal has a larger portion of δ waves with a larger amplitude [77]. This suggests that microstates are capable of extracting the similarities between sleep stages, while also retaining their differences.

6 Discussions and Conclusion

In this work, we introduce EEG microstates as a clinically grounded approach for integrating deep learning and EEG signal analysis.

Our approach improves the representation of brain activity by aligning more closely with the underlying neural mechanisms and cognitive activities, enhancing both clinical and research applications. Experimental results demonstrate the effectiveness of EEG microstates in three critical tasks—sleep staging, emotion recognition, and motor imagery classification and across different models, where it outperforms traditional time-domain and frequency-domain methods.

Furthermore, we show that EEG microstates present more performance gain than time- and frequency-domain features when scaling the data size, indicating that EEG microstates can alleviate

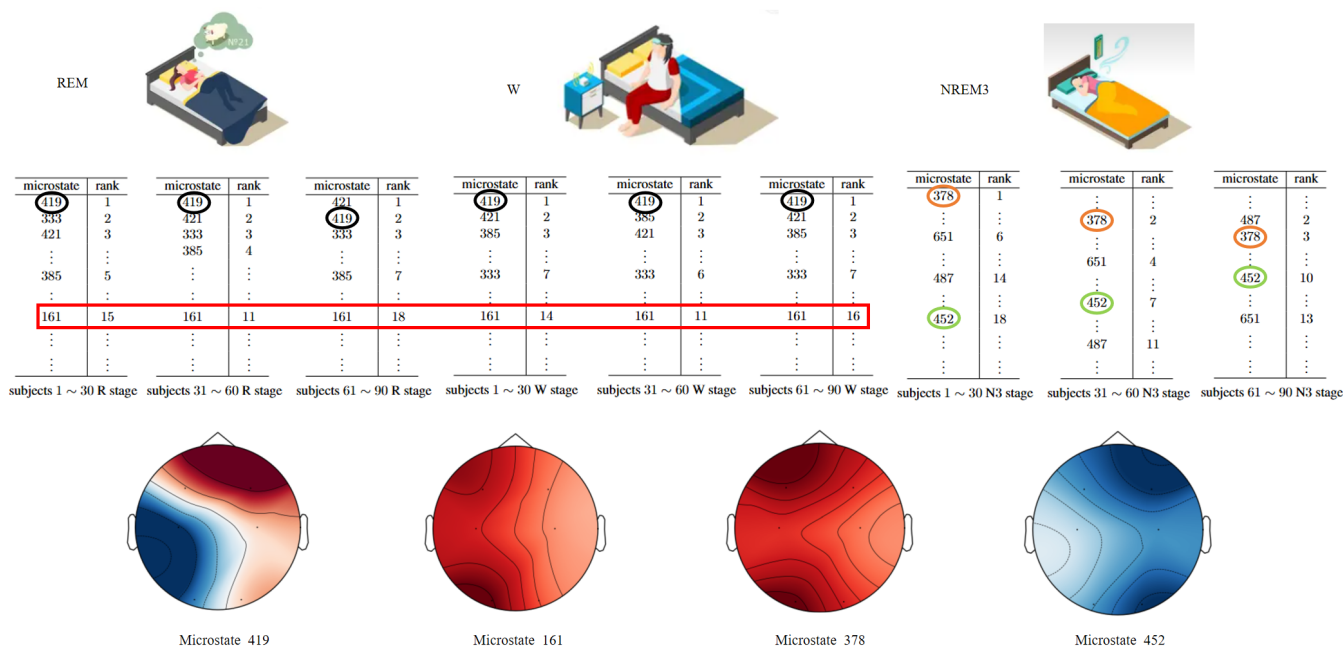


Figure 5: Visualizing Microstates Distribution. Visualization of the distribution of different microstates among different subjects undergoing different sleep stages. We can see that the microstate representation simultaneously retain the similarity between subjects and between W and R stage, while also preserves the difference between W stage N3 stage.

the burden of data scarcity and pave the way to more scalable settings. We also show that EEG microstates can provide interpretable insights for EEG analysis and deep learning, offering a promising direction for future research and clinical practice. The adoption of EEG microstates holds significant potential for advancing both cognitive neuroscience and the field of clinical diagnostics.

Several limitations guide future work, such as:

- We only experimented with limited tasks and limited number of datasets. Particularly, the training of the tokenizer was only performed on sleep data. This is reasonable because the HSP dataset is the largest, but more research can be conducted across tasks in the future.

- We only focused on the representation side. Based on the microstate representation, we hypothesize that it is possible to develop a pre-trained model that can generalize to several EEG-related downstream tasks.

Above all, we believe that combining deep learning techniques with biologically grounded EEG microstates opens up a portal to future research on improving the accuracy of EEG analysis across different tasks and on uncovering more correlations between microstates and brain activity. Future work might involve reconstructing brain signals with more channels to alleviate the lack of channel data.

References

- [1] Arshia Afzal, Grigorios Chrysos, Volkan Cevher, and Mahsa Shoaran. 2024. Rest: Efficient and accelerated eeg seizure analysis through residual state updates. *arXiv preprint arXiv:2406.16906* (2024).
- [2] Charu C. Aggarwal, Philip S. Yu, Jiawei Han, and Jianyong Wang. 2003. - A Framework for Clustering Evolving Data Streams. In *Proceedings 2003 VLDB Conference*, Johann-Christoph Freytag, Peter Lockemann, Serge Abiteboul, Michael Carey, Patricia Selinger, and Andreas Heuer (Eds.). Morgan Kaufmann, San Francisco, 81–92. doi:10.1016/B978-012722442-8/50016-1
- [3] David Ahmedt-Aristizabal, Tharindu Fernando, Simon Denman, Lars Petersson, Matthew J. Aburn, and Clinton Fookes. 2019. Neural Memory Networks for Seizure Type Classification. *2020 42nd Annual International Conference of the IEEE Engineering in Medicine & Biology Society (EMBC)* (2019), 569–575. <https://api.semanticscholar.org/CorpusID:210966442>
- [4] Aydin Akan and Ozlem Karabiber Cura. 2021. Time–frequency signal processing: Today and future. *Digital Signal Processing* 119 (2021), 103216. doi:10.1016/j.dsp.2021.103216
- [5] Irfan Al-Hussaini, Cao Xiao, M. Brandon Westover, and Jimeng Sun. 2019. SLEEPER: interpretable Sleep staging via Prototypes from Expert Rules. arXiv:1910.06100 [cs.LG] <https://arxiv.org/abs/1910.06100>
- [6] Ghita Amrani, Amina Adadi, Mohammed Berrada, Zouhayr Souirri, and Said Boujraf. 2021. EEG signal analysis using deep learning: A systematic literature review. In *2021 Fifth International Conference On Intelligent Computing in Data Sciences (ICDS)*, 1–8. doi:10.1109/ICDS53782.2021.9626707
- [7] Kleantlis Avramidis. 2021. Affective Analysis and Interpretation of Brain Responses to Music Stimuli.
- [8] Anahit Babayan, Miray Erbey, Deniz Kumral, Janis Reinelt, Andrea Reiter, Josefin Röbbig, H. Schaare, Marie Uhlig, Alfred Anwander, Pierre-Louis Bazin, Annette Horstmann, Leonie Lampe, Vadim Nikulin, Hadas Okon-Singer, Sven Preusser, André Pampel, Christiane Rohr, Julia Sacher, Angelika Thoene-Otto, and Arno Villringer. 2019. A mind-brain-body dataset of MRI, EEG, cognition, emotion, and peripheral physiology in young and old adults. *Scientific Data* 6 (02 2019), 180308. doi:10.1038/sdata.2018.308
- [9] Dongmei Bai, Tianshuang Qiu, and Xiaobing Li. 2007. [The sample entropy and its application in EEG based epilepsy detection]. *Sheng wu yi xue gong cheng xue za zhi = Journal of biomedical engineering = Shengwu yixue gongchengxue zazhi* 24 1 (2007), 200–5. <https://api.semanticscholar.org/CorpusID:21621951>
- [10] Juliane Britz, Dimitri Van De Ville, and Christoph M. Michel. 2010. BOLD correlates of EEG topography reveal rapid resting-state network dynamics. *NeuroImage* 52, 4 (2010), 1162–1170. doi:10.1016/j.neuroimage.2010.02.052
- [11] Verena Brodbeck, Alena Kuhn, Frederic von Wegner, Astrid Morzelewski, Enzo Tagliazucchi, Sergey Borisov, Christoph M. Michel, and Helmut Laufs. 2012. EEG microstates of wakefulness and NREM sleep. *NeuroImage* 62, 3 (2012), 2129–2139. doi:10.1016/j.neuroimage.2012.05.060
- [12] Zheng Chen, Ziwei Yang, Lingwei Zhu, Wei Chen, Toshiyo Tamura, Naoaki Ono, Md Altaf-Ul-Amin, Shigehiko Kanaya, and Ming Huang. 2023. Automated Sleep Staging via Parallel Frequency-Cut Attention. *IEEE Transactions on Neural Systems and Rehabilitation Engineering* 31 (2023), 1974–1985. doi:10.1109/TNSRE.2023.3243589
- [13] Joseph Y. Cheng, Hanlin Goh, Kaan Dogrusoz, Oncel Tuzel, and Erdin Azemi. 2020. Subject-Aware Contrastive Learning for Biosignals. *ArXiv abs/2007.04871* (2020). <https://api.semanticscholar.org/CorpusID:220425132>
- [14] Zhuoling Cheng, Xuekui Bu, Qingnan Wang, Tao Yang, and Jihui Tu. 2024. EEG-based emotion recognition using multi-scale dynamic CNN and gated transformer. *Scientific Reports* 14 (2024). <https://api.semanticscholar.org/CorpusID:275117639>
- [15] Ming Chu and Jingfeng Bi. 2023. Six classes of motor imagery EEG signals in the upper limb. doi:10.21227/8qw6-f578
- [16] Junyoung Chung, Caglar Gulcehre, KyungHyun Cho, and Yoshua Bengio. 2014. Empirical Evaluation of Gated Recurrent Neural Networks on Sequence Modeling. arXiv:1412.3555 [cs.NE] <https://arxiv.org/abs/1412.3555>
- [17] Jiayang Dong, Haixu Wu, Haoran Zhang, Li Zhang, Jianmin Wang, and Mingsheng Long. 2023. SimMTM: A Simple Pre-Training Framework for Masked Time-Series Modeling. In *Advances in Neural Information Processing Systems*, A. Oh, T. Naumann, A. Globerson, K. Saenko, M. Hardt, and S. Levine (Eds.), Vol. 36. Curran Associates, Inc., 29996–30025. https://proceedings.neurips.cc/paper_files/paper/2023/file/5f9bdfde3685e4ccdb0e7fb29cccf2a-Paper-Conference.pdf
- [18] Xiaobing Du, Cuixia Ma, Guanhua Zhang, Jinyao Li, Yu-Kun Lai, Guozhen Zhao, Xiaoming Deng, Yong-Jin Liu, and Hongan Wang. 2022. An Efficient LSTM Network for Emotion Recognition From Multichannel EEG Signals. *IEEE Transactions on Affective Computing* 13, 3 (2022), 1528–1540. doi:10.1109/TAFFC.2020.3013711
- [19] Ruo-Nan Duan, Jia-Yi Zhu, and Bao-Liang Lu. 2013. Differential entropy feature for EEG-based emotion classification. In *6th International IEEE/EMBS Conference on Neural Engineering (NER)*. IEEE, 81–84.
- [20] Robert Efron. 1970. The minimum duration of a perception. *Neuropsychologia* 8, 1 (1970), 57–63. doi:10.1016/0028-3932(70)90025-4
- [21] Abdeljalil El Hadiri, Lhoussain Bahatti, Abdelmounime El Magri, and Rachid Lajouad. 2024. Sleep stages detection based on analysis and optimisation of non-linear brain signal parameters. *Results in Engineering* 23 (2024), 102664. doi:10.1016/j.rineng.2024.102664
- [22] MohammadReza EskandariNasab, Zahra Raesi, Reza Ahmadi Lashaki, and Hamidreza Najafi. 2024. A GRU–CNN model for auditory attention detection using microstate and recurrence quantification analysis. *Scientific Reports* 14 (2024). <https://api.semanticscholar.org/CorpusID:269211640>
- [23] Shenzhi Fang, Chaofeng Zhu, Jinying Zhang, Luyan Wu, Yuying Zhang, Huapin Huang, and Wanhui Lin. 2024. EEG microstates in epilepsy with and without cognitive dysfunction: Alteration in intrinsic brain activity. *Epilepsy & Behavior* 154 (2024), 109729. doi:10.1016/j.yebeh.2024.109729
- [24] Linda Fiorini, Francesco Bossi, and Francesco Di Gruttola. 2024. EEG-based emotional valence and emotion regulation classification: a data-centric and explainable approach. *Scientific reports* 14, 1 (October 2024), 24046. doi:10.1038/s41598-024-75263-x
- [25] A. Goldberger, L. Amaral, L. Glass, J. Hausdorff, P. C. Ivanov, R. Mark, J. E. Mietus, G. B. Moody, Peng C. K., and H. E. Stanley. 2000. PhysioBank, PhysioToolkit, and PhysioNet: Components of a new research resource for complex physiologic signals. *Circulation* 101, 23 (2000), e215–e220. Online.
- [26] Xiaotong Gu, Zehong Cao, Alireza Jolfaei, Peng Xu, Dongrui Wu, Tzzy-Ping Jung, and Chin-Teng Lin. 2021. EEG-Based Brain-Computer Interfaces (BCIs): A Survey of Recent Studies on Signal Sensing Technologies and Computational Intelligence Approaches and Their Applications. *IEEE/ACM Transactions on Computational Biology and Bioinformatics* 18, 5 (2021), 1645–1666. doi:10.1109/TCCB.2021.3052811
- [27] Haokun Gui, Xiucheng Li, and Xinyang Chen. 2024. Vector Quantization Pre-training for EEG Time Series with Random Projection and Phase Alignment. In *Proceedings of the 41st International Conference on Machine Learning (Proceedings of Machine Learning Research, Vol. 235)*, Ruslan Salakhutdinov, Zico Kolter, Katherine Heller, Adrian Weller, Nuria Oliver, Jonathan Scarlett, and Felix Berkenkamp (Eds.). PMLR, 16731–16750. <https://proceedings.mlr.press/v235/gui24a.html>
- [28] Abir Hadriche, Laurent Pezard, Jean-Louis Nandrino, Hamadi Ghariani, Abdennaceur Kachouri, and Viktor K. Jirsa. 2013. Mapping the dynamic repertoire of the resting brain. *NeuroImage* 78 (2013), 448–462. doi:10.1016/j.neuroimage.2013.04.041
- [29] Jingzhao Hu, Chen Wang, Qiaomei Jia, Qirong Bu, Richard Sutcliffe, and Jun Feng. 2021. ScalingNet: Extracting features from raw EEG data for emotion recognition. *Neurocomputing* 463 (2021), 177–184. doi:10.1016/j.neucom.2021.08.018
- [30] Sunhee Hwang, Kibeom Hong, Guiyoung Son, and Hyeran Byun. 2020. Learning CNN features from DE features for EEG-based emotion recognition. *Pattern Analysis and Applications* 23, 3 (2020), 1323 – 1335. doi:10.1007/s10044-019-00860-w Cited by: 104.
- [31] Abhishek Iyer, Srimrit Sritik Das, Reva Teotia, Shishir Maheshwari, and Rishi Sharma. 2022. CNN and LSTM based Ensemble Learning for Human Emotion Recognition using EEG Recordings. *Multimedia Tools and Applications* (04 2022). doi:10.1007/s11042-022-12310-7
- [32] Smith K. Khare, Victoria Blanes-Vidal, Esmaeil S. Nadimi, and U. Rajendra Acharya. 2024. Emotion recognition and artificial intelligence: A systematic review (2014–2023) and research recommendations. *Information Fusion* 102 (2024), 102019. doi:10.1016/j.inffus.2023.102019
- [33] Domantė Kučikienė, Ravichandran Rajkumar, Katharina Timpte, Jan Heckelmann, Irene Neuner, Yvonne Weber, and Stefan Wolking. 2024. EEG microstates show different features in focal epilepsy and psychogenic nonepileptic seizures. *Epilepsia* 65 (01 2024). doi:10.1111/epi.17897
- [34] Byeong-Hoo Lee, Ji-Hoon Jeong, Kyung-Hwan Shim, and Dong-Joo Kim. 2020. Motor Imagery Classification of Single-Arm Tasks Using Convolutional Neural Network based on Feature Refining. arXiv:2002.01122 [cs.HC] <https://arxiv.org/abs/2002.01122>
- [35] D. Lehmann, H. Ozaki, and I. Pal. 1987. EEG alpha map series: brain micro-states by space-oriented adaptive segmentation. *Electroencephalography and Clinical Neurophysiology* 67, 3 (1987), 271–288. doi:10.1016/0013-4694(87)90025-3
- [36] D Lehmann, W.K Strik, B Hengeler, T Koenig, and M Koukhou. 1998. Brain electric microstates and momentary conscious mind states as building blocks of spontaneous thinking: I. Visual imagery and abstract thoughts. *International Journal of Psychophysiology* 29, 1 (1998), 1–11. doi:10.1016/S0167-8760(97)00098-6
- [37] Shuzhen Li, Yuxin Chen, Xuesong Chen, Ruiyang Gao, Yupeng Zhang, Chao Yu, Yunfei Li, Ziyi Ye, Weijun Huang, Hongliang Yi, et al. 2024. SleepNetZero: Zero-Burden Zero-Shot Reliable Sleep Staging with Neural Networks Based on Ballistocardiograms. *Proceedings of the ACM on Interactive, Mobile, Wearable and Ubiquitous Technologies* 8, 4 (2024), 1–25.
- [38] Robert Lin, Ren-Guey Lee, Chwan-Lu Tseng, Heng-Kuan Zhou, C. F. Chao, and Joe-Air Jiang. 2006. A NEW APPROACH FOR IDENTIFYING SLEEP APNEA SYNDROME USING WAVELET TRANSFORM AND NEURAL NETWORKS. *Biomedical Engineering: Applications, Basis and Communications* 18 (2006), 138–143. <https://api.semanticscholar.org/CorpusID:2412588>
- [39] Hong Liu, Haoling Tang, Wei Wei, Gesheng Wang, Yong Du, and Jianghai Ruan. 2021. Altered peri-seizure EEG microstate dynamics in patients with absence

- epilepsy. *Seizure* 88 (2021), 15–21. <https://api.semanticscholar.org/CorpusID:232359456>
- [40] Huisheng Lu, Mingshi Wang, and Hongqiang Yu. 2005. EEG Model and Location in Brain when Enjoying Music. *2005 IEEE Engineering in Medicine and Biology 27th Annual Conference* (2005), 2695–2698. <https://api.semanticscholar.org/CorpusID:21783113>
- [41] Marzia Lucia, Christoph Michel, Stephanie Clarke, and Micah Murray. 2007. Single-subject EEG analysis based on topographic information. *International Journal of Bioelectromagnetism* *www.ijbem.org* 9 (01 2007), 168–171.
- [42] Scott Makeig, Stefan Debener, Julie Onton, and Arnaud Delorme. 2004. Mining event-related brain dynamics. *Trends in Cognitive Sciences* 8, 5 (2004), 204–210. doi:10.1016/j.tics.2004.03.008
- [43] Christoph M. Michel and Thomas Koenig. 2018. EEG microstates as a tool for studying the temporal dynamics of whole-brain neuronal networks: A review. *NeuroImage* 180 (2018), 577–593. doi:10.1016/j.neuroimage.2017.11.062 Brain Connectivity Dynamics.
- [44] P. Milz, P.L. Faber, D. Lehmann, T. Koenig, K. Kochi, and R.D. Pascual-Marqui. 2016. The functional significance of EEG microstates—Associations with modalities of thinking. *NeuroImage* 125 (2016), 643–656. doi:10.1016/j.neuroimage.2015.08.023
- [45] Micah Murray, Denis Brunet, and Christoph Michel. 2008. Topographic ERP Analyses: A Step-by-Step Tutorial Review. *Brain topography* 20 (07 2008), 249–64. doi:10.1007/s10548-008-0054-5
- [46] Yuqi Nie, Nam H. Nguyen, Phanwadee Sinthong, and Jayant Kalagnanam. 2022. A Time Series is Worth 64 Words: Long-term Forecasting with Transformers. *ArXiv abs/2211.14730* (2022). <https://api.semanticscholar.org/CorpusID:254044221>
- [47] R.D. Pascual-Marqui, C.M. Michel, and D. Lehmann. 1995. Segmentation of brain electrical activity into microstates: model estimation and validation. *IEEE Transactions on Biomedical Engineering* 42, 7 (1995), 658–665. doi:10.1109/10.391164
- [48] Mathias Perslev, S. Darkner, Lykke Kempfner, Miki Nikolic, Poul Jørgen Jennum, and C. Igel. 2021. U-Sleep: resilient high-frequency sleep staging. *NPJ Digital Medicine* 4 (2021). <https://api.semanticscholar.org/CorpusID:15084282>
- [49] Huy Phan, Kaare Mikkelsen, Oliver Y. Chen, Philipp Koch, Alfred Mertins, and Maarten De Vos. 2022. SleepTransformer: Automatic Sleep Staging With Interpretability and Uncertainty Quantification. *IEEE Transactions on Biomedical Engineering* 69, 8 (2022), 2456–2467. doi:10.1109/TBME.2022.3147187
- [50] Gilles Pourtois, Sylvain Delplanque, Christoph M. Michel, and Patrik Vuilleumier. 2008. Beyond Conventional Event-related Brain Potential (ERP): Exploring the Time-course of Visual Emotion Processing Using Topographic and Principal Component Analyses. *Brain Topography* 20 (2008), 265–277. <https://api.semanticscholar.org/CorpusID:15084282>
- [51] Giulia Prete, Pierpaolo Croce, Filippo Zappasodi, Luca Tommasi, and Paolo Capotosto. 2022. Exploring brain activity for positive and negative emotions by means of EEG microstates. *Scientific Reports* 12 (03 2022), 1–11. doi:10.1038/s41598-022-07403-0
- [52] Asha S.A, Sudalaimani C, Devanand P, Alexander G, Arya Maniyan Lathikakumari, Sanjeev V Thomas, and Ramshekhhar N Menon. 2024. Analysis of EEG microstates as biomarkers in neuropsychological processes – Review. *Computers in Biology and Medicine* 173 (2024), 108266. doi:10.1016/j.combiomed.2024.108266
- [53] G. Schalk, D.J. McFarland, T. Hinterberger, N. Birbaumer, and J.R. Wolpaw. 2004. BCI2000: a general-purpose brain-computer interface (BCI) system. *IEEE Transactions on Biomedical Engineering* 51, 6 (2004), 1034–1043. doi:10.1109/TBME.2004.827072
- [54] Bastian Schiller, Matthias Sperl, Tobias Kleinert, Kyle Nash, and Lorena Gianotti. 2023. EEG Microstates in Social and Affective Neuroscience. *Brain Topography* 37 (07 2023), 1–17. doi:10.1007/s10548-023-00987-4
- [55] Felix Schlegel, D. Lehmann, Pascal Faber, Patricia Milz, and Lorena Gianotti. 2011. EEG Microstates During Resting Represent Personality Differences. *Brain topography* 25 (06 2011), 20–6. doi:10.1007/s10548-011-0189-7
- [56] Benjamin A. Seitzman, Malene Abell, Samuel C. Bartley, Molly A. Erickson, Amanda R. Bolbecker, and William P. Hetrick. 2017. Cognitive manipulation of brain electric microstates. *NeuroImage* 146 (2017), 533–543. doi:10.1016/j.neuroimage.2016.10.002
- [57] Xiaorui Shao and Chang Soo Kim. 2022. A Hybrid Deep Learning Scheme for Multi-Channel Sleep Stage Classification. *Computers, Materials & Continua* (2022). <https://api.semanticscholar.org/CorpusID:243464227>
- [58] Xinke Shen, Xianggen Liu, Xin Hu, Dan Zhang, and Sen Song. 2023. Contrastive Learning of Subject-Invariant EEG Representations for Cross-Subject Emotion Recognition. *IEEE Transactions on Affective Computing* 14, 3 (2023), 2496–2511. doi:10.1109/TAFFC.2022.3164516
- [59] In-Ho Song, Doo-Soo Lee, and Sun I Kim. 2004. Recurrence quantification analysis of sleep electroencephalogram in sleep apnea syndrome in humans. *Neuroscience Letters* 366, 2 (2004), 148–153. doi:10.1016/j.neulet.2004.05.025
- [60] Tengfei Song, Suyuan Liu, Wenming Zheng, Yuan Zong, Zhen Cui, Yang Li, and Xiaoyan Zhou. 2021. Variational Instance-Adaptive Graph for EEG Emotion Recognition. *IEEE Transactions on Affective Computing* 14 (2021), 343–356. <https://api.semanticscholar.org/CorpusID:233621668>
- [61] Jianlin Su, Yu Lu, Shengfeng Pan, Ahmed Murtadha, Bo Wen, and Yunfeng Liu. 2023. RoFormer: Enhanced Transformer with Rotary Position Embedding. arXiv:2104.09864 [cs.CL] <https://arxiv.org/abs/2104.09864>
- [62] D. Puthankattil Subha, Paul K. Joseph, Rajendra Acharya U., and Choo Min Lim. 2010. EEG Signal Analysis: A Survey. *Journal of Medical Systems* 34 (2010), 195–212. <https://api.semanticscholar.org/CorpusID:1140473>
- [63] Luke Tait, Francesco Tamagnini, George Stothart, Edoardo Barvas, Chiara Monaldini, Roberto P Frusciant, Mirco Volpini, Susanna Guttman, Elizabeth J. Coulthard, Jon T. Brown, Nina Kazanina, and Marc Goodfellow. 2019. EEG microstate complexity for aiding early diagnosis of Alzheimer’s disease. *Scientific Reports* 10 (2019). <https://api.semanticscholar.org/CorpusID:209578713>
- [64] Padhmashree V. and Abhijit Bhattacharyya. 2022. Human emotion recognition based on time–frequency analysis of multivariate EEG signal. *Knowledge-Based Systems* 238 (2022), 107867. doi:10.1016/j.knsys.2021.107867
- [65] V. Vanitha and P. Krishnan. 2017. Time-frequency analysis of EEG for improved classification of emotion. *International Journal of Biomedical Engineering and Technology* 23, 2-4 (2017), 191–212. arXiv:https://www.inderscienceonline.com/doi/pdf/10.1504/IJBET.2017.082661 doi:10.1504/IJBET.2017.082661
- [66] Anna Elisabetta Vaudano, Nicoletta Azzi, and Irene Trippi. 2019. *Normal Sleep EEG*. Springer International Publishing, Cham, 153–175. doi:10.1007/978-3-030-04573-9_10
- [67] Neeraj Wagh, Jionghao Wei, Samarth Rawal, Brent M. Berry, and Yogatheesan Varatharajah. 2022. Evaluating Latent Space Robustness and Uncertainty of EEG-ML Models under Realistic Distribution Shifts. arXiv:2209.11233 [eess.SP] <https://arxiv.org/abs/2209.11233>
- [68] Fei Wang, Shichao Wu, Weiwei Zhang, Zongfeng Xu, Yahui Zhang, Chengdong Wu, and Sonya Coleman. 2020. Emotion recognition with convolutional neural network and EEG-based EFDs. *Neuropsychologia* 146 (2020), 107506. doi:10.1016/j.neuropsychologia.2020.107506
- [69] Guangyu Wang, Wenchao Liu, Yuhong He, Cong Xu, Lin Ma, and Haifeng Li. 2024. EEGPT: Pretrained Transformer for Universal and Reliable Representation of EEG Signals. In *The Thirty-eighth Annual Conference on Neural Information Processing Systems*.
- [70] Jiquan Wang, Sha Zhao, Haiteng Jiang, Shijian Li, Tao Li, and Gang Pan. 2024. Generalizable Sleep Staging via Multi-Legal Domain Alignment. arXiv:2401.05363 [eess.SP] <https://arxiv.org/abs/2401.05363>
- [71] Xiao-Wei Wang, Dan Nie, and Bao-Liang Lu. 2011. EEG-Based Emotion Recognition Using Frequency Domain Features and Support Vector Machines. In *International Conference on Neural Information Processing*. <https://api.semanticscholar.org/CorpusID:9355572>
- [72] Yiming Wang, Bin Zhang, and Yujiao Tang. 2024. DMMR: Cross-Subject Domain Generalization for EEG-Based Emotion Recognition via Denoising Mixed Mutual Reconstruction. In *AAAI Conference on Artificial Intelligence*. <https://api.semanticscholar.org/CorpusID:268678230>
- [73] M. B. Westover, V. Moura Junior, R. Thomas, S. Cash, S. Nasiri, H. Sun, A. Gupta, J. Rosand, M. Ghanta, W. Ganglberger, U. Katwa, K. Stone, Z. Zhang, G. Ganjoo, T. E. Nassi PhD Candidate, R. Wei, D. Hwang, L. M. Trotti, A. Parekh, E. Meulenbrugge, E. Mignot, R. Au, G. Clifford, and D. Rapoport. 2023. The Human Sleep Project (version 2.0). *Brain Data Science Platform*. <https://doi.org/10.60508/qjvb-hg78>.
- [74] Haixu Wu, Teng Hu, Yong Liu, Hang Zhou, Jianmin Wang, and Mingsheng Long. 2022. TimesNet: Temporal 2D-Variation Modeling for General Time Series Analysis. *ArXiv abs/2210.02186* (2022). <https://api.semanticscholar.org/CorpusID:252715491>
- [75] Guowen Xiao, Mengwen Ye, Bowen Xu, Zhendi Chen, and Quansheng Ren. 2021. 4D Attention-based Neural Network for EEG Emotion Recognition. arXiv:2101.05484 [cs.LG] <https://arxiv.org/abs/2101.05484>
- [76] Chen Zechuan and Zhang Kan. 2024. *The Principles of Psychology*. Springer Nature Singapore, Singapore, 1–2. doi:10.1007/978-981-99-6000-2_1042-1
- [77] Xiaoli Zhang, Xizhen Zhang, Qiong Huang, Yang Lv, and Fuming Chen. 2024. A review of automated sleep stage based on EEG signals. *Biocybernetics and Biomedical Engineering* 44, 3 (2024), 651–673. doi:10.1016/j.bbe.2024.06.004
- [78] Jingyi Zheng, Mingli Liang, Sujata Sinha, Linqiang Ge, Wei Yu, Arne Ekstrom, and Fushing Hsieh. 2022. Time-Frequency Analysis of Scalp EEG With Hilbert-Huang Transform and Deep Learning. *IEEE Journal of Biomedical and Health Informatics* 26, 4 (2022), 1549–1559. doi:10.1109/JBHI.2021.3110267
- [79] Wei-Long Zheng and Bao-Liang Lu. 2015. Investigating Critical Frequency Bands and Channels for EEG-based Emotion Recognition with Deep Neural Networks. *IEEE Transactions on Autonomous Mental Development* 7, 3 (2015), 162–175. doi:10.1109/TAMD.2015.2431497
- [80] Xinliang Zhou, Chenyu Liu, Zhongruo Wang, Liming Zhai, Ziyu Jia, Cuntai Guan, and Yang Liu. 2024. Interpretable and Robust AI in EEG Systems: A Survey. arXiv:2304.10755 [eess.SP] <https://arxiv.org/abs/2304.10755>
- [81] Ning Zhuang, Ying Zeng, li Tong, Chi Zhang, Hanming Zhang, and Bin Yan. 2017. Emotion Recognition from EEG Signals Using Multidimensional Information in EMD Domain. *BioMed Research International* 2017 (08 2017), 1–9. doi:10.1155/2017/8317357

Acknowledgments

This work is supported by the Ministry of Science and Technology of China STI2030-Major Projects (No. 2021ZD0201900, 2021ZD0201902). The computations in this research were performed using the CFFF platform of Fudan University.

A Experimental Setup

This section gives the detailed experimental configuration of our downstream tasks.

A.1 Sleep Staging

A.1.1 Dataset. The dataset used is the **Human Sleep Project (HSP)** dataset [73]. This dataset includes PSG signals from over 20K subjects. Signals are sampled under various frequencies including 256Hz and 512Hz. Each sample includes a night’s sleep of a subject sampled, with sleep stages annotated every 30 seconds. Equivalently, we have the raw EEG signals $s \in \mathbb{R}^{C \times f_s T}$ where C consists of different classes of channels such as EOG, ECG, and EEG and differs across subjects, f_s denotes the sample frequency which also differs across subjects, and T is the time duration of a night’s sleep, which is typically 6-7 hours. The label frequency is $f_l = \frac{1}{30}$ Hz.

A.1.2 Preprocessing.

Extracting target channels. As for constructing the microstates, we have to filter out a fixed number of channels. To achieve this goal, we extract $N = 6$ channels which is common among all samples. The EEG leads are shown in the following diagram [19, 79]. The channels chosen are F3, F4, C3, C4, O1, O2. After extraction, the EEG signals have shape $s_{ext} \in \mathbb{R}^{N \times f_s T}$.

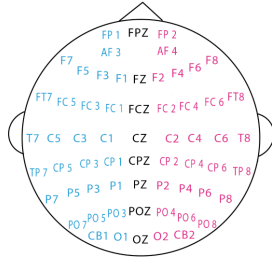


Figure 6: The Distribution of EEG Leads

Filtering and Resampling. The raw EEG signals are then bandpass filtered between 1Hz and 40Hz, followed by a resampling at $f_{res} = 100$ Hz. After these procedures, the raw EEG signals now have shape $s_{res} \in \mathbb{R}^{N \times f_{res} T}$. Having obtained the resampled data, we construct the representations accordingly.

Constructing microstates. The fitted clustering model is applied to the resampled data $s_{res} \in \mathbb{R}^{N \times f_{res} T}$. The result is a microstate sequence $c \in S^{f_{res} T}$ where $S \in \{b_1, b_2, \dots, b_k\}$ is a set of k discrete states. Here we let $k = 1000$.

Constructing baseline. We directly use the raw EEG signals for time-domain features. The input shape is $s_{time} \in \mathbb{R}^{N \times f_{res} T}$.

To extract frequency information, we use short-time Fourier transform. The major goal is to decompose the signal into powers

at different frequencies. [4]. For a given frequency f , the power is computed as follows:

$$X(t, f) = \int_{-\infty}^{\infty} w(t - \tau) s(\tau) e^{-i2\pi f \tau} d\tau$$

$$p(t, f) = \frac{1}{2\pi} |X(t, f)|^2$$

where $w(t)$ is a window function. Note that

$$X'(t, f) = \int_{-\infty}^{\infty} s(\tau) e^{-i2\pi f \tau} d\tau$$

is the usual Fourier transform, and the window function $w(t)$ only has finite support which serves as a short-time weighted sum of the integral. We use the Hann window function defined as follows:

$$w(t) = \begin{cases} \frac{1}{2} \left(1 - \cos \frac{2\pi t}{T}\right) & |t| \leq \frac{T}{2} \\ 0 & |t| > \frac{T}{2} \end{cases}$$

where T is the window length. In our setting we set $T = t_w = 1$ s. The overlap ratio is set to be $r_o = 0$.

Using the above approach, the processed frequency-domain signals have length l' where

$$l' = \left\lceil \frac{f_{res} T - f_{res} t_w}{(1 - r_o) f_{res} t_w} \right\rceil + 1$$

is the number of windows. Leaving out the margin, we have that

$$l' = \frac{T}{(1 - r_o) t_w} = f_{freq} T$$

here for $r_o = 0$ and $t_w = 1$ s, we have $f_{freq} = 1$ Hz.

Having calculated the power $p(t, f)$ at frequency f and time t , we obtain the spectrogram $P \in \mathbb{R}^{F \times f_{freq} T}$ for each channel, where F is the frequency axis and $f_{freq} T$ is the time axis.

Next, we apply band integration. Human EEG signal is divided into the following frequency bands:

- δ -band: 0.5 ~ 4Hz
- θ -band: 4 ~ 8Hz
- α -band: 8 ~ 12Hz
- σ -band: 12 ~ 16Hz
- β -band: 16 ~ 30Hz
- γ -band: 30 ~ 40Hz

and we combine the powers among F within each band. We use simpson integration as our numerical quadrature method, which is defined as

$$\int_a^b f(x) dx = \frac{b-a}{6} \left(f(a) + 4f\left(\frac{a+b}{2}\right) + f(b) \right)$$

for a step interval $[a, b]$. After the integration, the array shape becomes $s_{freq, sin} \in \mathbb{R}^{B \times f_{freq} T}$ where $B = 6$ is the number of bands.

As our final step, we flatten the array for each channel to $s_{freq, sin, flat} \in \mathbb{R}^{B f_{freq} T}$ and stack the N channels together, resulting in shape $s_{freq} \in \mathbb{R}^{N \times B f_{freq} T}$.

Slicing. We select fixed window size $T_w = 300$ s. In this case, a microstates sample will have shape $c_w \in S^{f_{res} T_w} = S^{30000}$, and the raw EEG data will have shape $s_{time, w} \in \mathbb{R}^{N \times f_{res} T_w} = \mathbb{R}^{6 \times 30000}$. The frequency-domain representation will have shape $s_{freq, w} \in \mathbb{R}^{N \times B f_{freq} T_w} = \mathbb{R}^{6 \times 1800}$.

A.1.3 *Labels.* The label frequency is $f_l = \frac{1}{30}$ Hz, and hence the label sequence will be of shape $l_w \in L^{f_l T_w} = L^{10}$ where L consists of the five sleep stages.

A.2 Emotion Recognition

A.2.1 *Dataset.* The dataset used is the **SEED** dataset [19, 79]. The SEED dataset consists of 15 subjects whose EEG signals of 62 channels are recorded when watching movie clips expressing different emotions which are categorized as positive, neutral and negative. There are a total number of 15 trials, during which subjects view episodes with positive, neutral, negative, negative, neutral, positive, negative, neutral, positive, positive, neutral, negative, neutral, positive, negative emotions. The dataset is filtered between 0 and 75Hz and downsampled to 200Hz. In raw EEG samples have shape $s \in \mathbb{R}^{C \times f_s T}$ where $f_s = 200$ Hz and $C = 62$. T is the length of the movie clip which varies between trials.

A.2.2 *Preprocessing.*

Extracting target channels. We extract the 6 target channels as above for labeling. The resulting shape is $s_{ext} \in \mathbb{R}^{N \times f_s T}$ where $N = 6$.

Constructing microstates and baseline. We do not filter and re-sample the EEG signals since these are done initially. Applying the clustering model, we obtain the microstate sequence $c \in S^{f_s T}$ where S is the set of 1000 states. The raw signal has shape $s_{time} \in \mathbb{R}^{N \times f_s T}$, and the frequency-domain signal has shape $s_{freq} \in \mathbb{R}^{N \times B f_{freq} T}$ where $f_{freq} = 1$ Hz and $B = 6$ is the number of bands.

Windowing. Since the movie clips are not of the same length, we set $T_w = 265$ s which is the duration of the longest video, and pad the signals that are shorter. For microstates, a new token is introduced for padding, whereas for the other two representations, we pad zeros. Now the microstate sequence has length $f_s T_w = 53000$, the raw EEG signals have shape $s_{time,w} \in \mathbb{R}^{N \times f_s T_w} = \mathbb{R}^{6 \times 53000}$ and the frequency-domain signals have shape $s_{freq,w} \in \mathbb{R}^{6 \times 1590}$.

A.2.3 *Labels.* As mentioned in [7], human emotions can be characterized in the valence-arousal space as in Figure 7. Valence and arousal are two dominant factors categorizing human feelings. Since the SEED dataset only features the valence aspect, the prediction of emotions is focused on the valence component, with labels L defined as positive, neutral and negative. Each segmented window corresponds to a single emotion label.

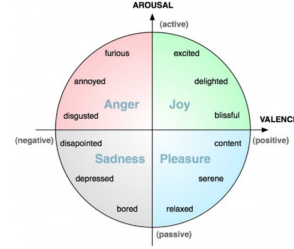


Figure 7: The Valence-Arousal Space

A.3 Motor Imagery Classification

A.3.1 *Dataset.* We use the **Motor Movement/Imagery** dataset [25, 53]. The dataset consists of 109 subjects undergoing 14 trials. The 14 trials includes two rest sessions and four tasks. The four tasks are:

- Task 1: Open and close the left or right fist.
- Task 2: Imagine opening and closing the left or right fist.
- Task 3: Open and close both fists or both feet.
- Task 4: Imagine opening and closing both fists or feet.

Every subject went through two rest sessions and three rounds of successive tasks in the order above. The labels are given during movement roughly every four seconds. There are in total three labels. T_0 corresponds to rest, T_1 corresponds to the onset of moving or imagining moving the left or both fists, and T_2 corresponds to the onset of moving or imagining moving the right fist or both feet. The samples contain 64 channels at $f_s = 160$ Hz. In this case, the raw EEG signals have shape $s \in \mathbb{R}^{C \times f_s T}$ where $C = 64$, $f_s = 160$ Hz and T is the duration of each trial.

A.3.2 *Preprocessing.*

Extracting target channels. Again, the six target channels are extracted and the resulting shape is $s_{ext} \in \mathbb{R}^{N \times f_s T}$, $N = 6$.

Constructing microstates and baseline. We directly apply the clustering model on the raw EEG and obtain the microstate sequence $c \in S^{f_s T}$. The raw EEG signals have shape $s_{time} \in \mathbb{R}^{N \times f_s T}$ and the frequency-domain signals have shape $s_{freq} \in \mathbb{R}^{N \times B f_{freq} T}$ where $f_{freq} = 1$ Hz.

Slicing. Since each label lasts for roughly 4s. We set $T_w = 4$ s. And thus the microstate sequence has length 640, the raw EEG signal has shape $s_{time,w} \in \mathbb{R}^{6 \times 640}$ where as the frequency-domain signal has shape $s_{freq,w} \in \mathbb{R}^{6 \times 24}$.

A.3.3 *Labels.* We let L consists of four labels: left hand, right hand, both hands, both feet. Left hand corresponds to the label T_1 in trials 3, 4, 7, 8, 11, 12, right hand corresponds to the label T_2 in trials 3, 4, 7, 8, 11, 12, both hands corresponds to the label T_1 in trials 5, 6, 9, 10, 13, 14 and both feet corresponds to the label T_2 in trials 5, 6, 9, 10, 13, 14. Each sample corresponds to a single movement label.

B Model Architecture and Training

This section shows the detailed model structures adopted in this work.

B.1 CNN+LSTM [57]

B.1.1 Model Details.

Overview of model structure. The following shows the model structure. The three models have parameters 707K, 692K and 687K respectively. Models are shown in Table 3, Table 4 and Table 5.

CNN and GRU. The convolution layers are employed to extract the spatial information across channels, and the gated recurrent units (GRUs) are used to extract temporal information.

GRU is a simplified version of long short term memory (LSTM) [16]. It consists of two gates—the update gate z and the reset gate r .

At each time step t , the activation of the update gate z_t is computed as

$$z_t = \sigma(W_z \mathbf{x}_t + U_z \mathbf{h}_{t-1})$$

where \mathbf{h}_{t-1} is the activation of the GRU at time step $t - 1$ and σ denotes the element-wise sigmoid function. Similarly, the activation r_t of the reset gate is computed as

$$r_t = \sigma(W_r \mathbf{x}_t + U_r \mathbf{h}_{t-1})$$

Next, the candidate activate $\tilde{\mathbf{h}}_t$ is computed as

$$\tilde{\mathbf{h}}_t = \tanh(W \mathbf{x}_t + \mathbf{r}_t^T U \mathbf{h}_{t-1})$$

The activation \mathbf{h}_t at time step t is computed as

$$\mathbf{h}_t = (\mathbf{1}^T - z_t^T) \mathbf{h}_{t-1} + z_t^T \tilde{\mathbf{h}}_{t-1}$$

Using this mechanism, the model can selectively consider input at different time steps.

Embedding layer. To adapt the model simultaneously to continuous and discrete EEG representations, we use different layers for microstates and conventional representations. For microstates, an embedding layer is adopted to convert discrete microstates into high-dimensional vectors, and for continuous signals, we use a convolution layer, which functions similarly by mapping the input into a high-dimensional latent space. The dimensions are chosen appropriately to guarantee that the model parameters are roughly the same.

B.1.2 Training Configuration. This section lists the training configurations of the above 3 models in Table 6. The models are trained on an NVIDIA-H20 GPU. The parameters in each case is optimized for performance and memory utilization.

B.2 Sleep Transformer [49]

B.2.1 Model Details.

Overview of model structure. The following shows the model structure of Sleep Transformer. Parameters are 3.2M, 3.2M and 3.4M, respectively. Model structures are shown in Table 7, Table 8 and Table 9.

RoFormer. The main part of the model uses an attention-based mechanism to extract temporal features. RoFormer is proposed in [61], which utilizes a novel positional embedding.

Generally speaking, the attention mechanism needs a key \mathbf{k}_i , query \mathbf{q}_i and value \mathbf{v}_i for each input position i . We can write them as

$$\mathbf{q}_i = f_q(\mathbf{x}_i, i)$$

$$\mathbf{k}_i = f_k(\mathbf{x}_i, i)$$

$$\mathbf{v}_i = f_v(\mathbf{x}_i, i)$$

where \mathbf{x}_i is the word vector at position i . The attention between position m, n is calculated as

$$a_{m,n} = \frac{e^{\frac{\mathbf{q}_m^T \mathbf{k}_n}{\sqrt{d}}}}{\sum_{j=1}^N e^{\frac{\mathbf{q}_m^T \mathbf{k}_j}{\sqrt{d}}}}$$

and since this value is calculated in parallel, we have to incorporate the positional information i along with \mathbf{x}_i into the queries and keys.

The main idea of RoFormer is to select a positional embedding such that

$$\mathbf{q}_m^T \mathbf{k}_n = g(\mathbf{x}_m, \mathbf{x}_n, n - m)$$

is a function that depends solely on the input word vector and the relative position between m, n .

To construct such a positional embedding, let the embedding dimension be d which is an even number, then we construct the following matrix

$$\mathbf{R}_{\Theta, m}^d = \begin{pmatrix} \cos m\theta_1 & -\sin m\theta_1 & \dots & 0 & 0 \\ \sin m\theta_1 & \cos m\theta_1 & \dots & 0 & 0 \\ 0 & 0 & \dots & 0 & 0 \\ 0 & 0 & \dots & 0 & 0 \\ \vdots & \vdots & \ddots & \vdots & \vdots \\ 0 & 0 & \dots & \cos m\theta_{\frac{d}{2}} & -\sin m\theta_{\frac{d}{2}} \\ 0 & 0 & \dots & \sin m\theta_{\frac{d}{2}} & \cos m\theta_{\frac{d}{2}} \end{pmatrix}$$

and we have

$$\mathbf{q}_m = \mathbf{R}_{\Theta, m}^d \mathbf{W}_q \mathbf{x}_m$$

$$\mathbf{k}_n = \mathbf{R}_{\Theta, n}^d \mathbf{W}_k \mathbf{x}_k$$

$$\mathbf{q}_m^T \mathbf{k}_n = \mathbf{x}_m^T \mathbf{W}_q^T \mathbf{R}_{\Theta, n-m}^d \mathbf{W}_k \mathbf{x}_k = g(\mathbf{x}_m, \mathbf{x}_n, n - m)$$

Embedding layer. An embedding layer is added before the microstates model. There are 2 extra vectors for padding and classification token. A convolution layer is used instead for continuous signals.

B.2.2 Training Configuration. The models are trained on an NVIDIA-H20 GPU. Parameters are optimized for performance and memory utilization.

B.3 Sleep Net Zero [37]

B.3.1 Model Details.

Overview of model structure. The following shows the model structure of Sleep Net Zero. Parameters are 10.9M, 3.2M and 3.2M. Model details are shown in Table 12, Table 13 and Table 14.

Embedding layer. We adopt an embedding layer with 1002 tokens for microstates. For raw EEG signals, since its input size is significantly larger than the other two representations, we increase the embedding dimension for better performance.

Table 5: CNN+LSTM for Raw EEG

LAYER	OUTPUT	CONFIGURATION
–	(6, 30000)	–
CONV1D	(1024, 30000)	INPUT CHANNELS 6, OUTPUT CHANNELS 1024, KERNEL SIZE 5 PADDING 2
BATCHNORM1D	(1024, 30000)	1024
CONV1D	(128, 10000)	INPUT CHANNELS 1024, OUTPUT CHANNELS 128, KERNEL SIZE 3 STRIDE 3
MAXPOOL1D	(128, 5000)	KERNEL SIZE 2, STRIDE 2
DROPOUT	(128, 5000)	$p = 0.25$
CONV1D	(64, 1000)	INPUT CHANNELS 128, OUTPUT CHANNELS 64, KERNEL SIZE 5 STRIDE 5
MAXPOOL1D	(64, 500)	KERNEL SIZE 2, STRIDE 2
DROPOUT	(64, 500)	$p = 0.25$
CONV1D	(32, 500)	INPUT CHANNELS 64, OUTPUT CHANNELS 32, KERNEL SIZE 3 PADDING 1
MAXPOOL1D	(32, 250)	KERNEL SIZE 2, STRIDE 2
DROPOUT	(32, 250)	$p = 0.25$
GRU	(64, 250)	INPUT SIZE 32, HIDDEN SIZE 64, 2 LAYERS
DROPOUT	(64, 250)	$p = 0.25$
GRU	(128, 250)	INPUT SIZE 64, HIDDEN SIZE 128, 2 LAYERS
DROPOUT	(128, 250)	$p = 0.25$
RESHAPE	(10, 3200)	–
LINEAR	(10, 5)	INPUT FEATURES 3200, OUTPUT FEATURES 5

Table 6: CNN+LSTM for Frequency-Domain

LAYER	OUTPUT	CONFIGURATION
–	(6, 1800)	–
CONV1D	(1024, 1800)	INPUT CHANNELS 6, OUTPUT CHANNELS 1024, KERNEL SIZE 5 PADDING 2
BATCHNORM1D	(1024, 1800)	1024
CONV1D	(128, 600)	INPUT CHANNELS 1024, OUTPUT CHANNELS 128, KERNEL SIZE 3 STRIDE 3
MAXPOOL1D	(128, 300)	KERNEL SIZE 2, STRIDE 2
DROPOUT	(128, 300)	$p = 0.25$
CONV1D	(64, 60)	INPUT CHANNELS 128, OUTPUT CHANNELS 64, KERNEL SIZE 5 STRIDE 5
MAXPOOL1D	(64, 30)	KERNEL SIZE 2, STRIDE 2
DROPOUT	(64, 30)	$p = 0.25$
CONV1D	(32, 30)	INPUT CHANNELS 64, OUTPUT CHANNELS 32, KERNEL SIZE 3 PADDING 1
MAXPOOL1D	(32, 15)	KERNEL SIZE 2, STRIDE 2
DROPOUT	(32, 15)	$p = 0.25$
GRU	(64, 15)	INPUT SIZE 32, HIDDEN SIZE 64, 2 LAYERS
DROPOUT	(64, 15)	$p = 0.25$
GRU	(128, 15)	INPUT SIZE 64, HIDDEN SIZE 128, 2 LAYERS
DROPOUT	(128, 15)	$p = 0.25$
RESHAPE	(10, 192)	–
LINEAR	(10, 5)	INPUT FEATURES 192, OUTPUT FEATURES 5

B.3.2 Training Configuration. The models are trained on an NVIDIA-H20 GPU. Parameters in each case are optimized for performance and memory utilization.

B.4 CNN-Based Model for Emotion Recognition [13]

Apart from sleep staging, we show the model used for emotion recognition.

B.4.1 Model Details.

Overview of model structure. The following shows the model structure of the CNN-based model. Parameters are 19.1M, 19.1M and 20.1M. Model details are shown in Table 16, Table 17 and Table 18.

Embedding layer. For microstates, an embedding layer with vocabulary 1001 and dimension 1024 is employed. The extra token is for padding. Convolution layers are used in the place of embedding for the other two representations.

Table 7: CNN+LSTM for Microstates

LAYER	OUTPUT	CONFIGURATION
-	(30000,)	-
EMBEDDING	(30000, 512)	NUMBER OF EMBEDDINGS 1000, DIMENSION 512
TRANSPOSE	(512, 30000)	-
BATCHNORM1D	(512, 30000)	512
CONV1D	(64, 10000)	INPUT CHANNELS 512, OUTPUT CHANNELS 64, KERNEL SIZE 3 STRIDE 3
MAXPOOL1D	(64, 5000)	KERNEL SIZE 2, STRIDE 2
DROPOUT	(64, 5000)	$p = 0.25$
CONV1D	(32, 1000)	INPUT CHANNELS 64, OUTPUT CHANNELS 32, KERNEL SIZE 5 STRIDE 5
MAXPOOL1D	(32, 500)	KERNEL SIZE 2, STRIDE 2
DROPOUT	(32, 500)	$p = 0.25$
CONV1D	(16, 500)	INPUT CHANNELS 32, OUTPUT CHANNELS 16, KERNEL SIZE 3 PADDING 1
MAXPOOL1D	(16, 250)	KERNEL SIZE 2, STRIDE 2
DROPOUT	(16, 250)	$p = 0.25$
GRU	(32, 250)	INPUT SIZE 16, HIDDEN SIZE 32, 2 LAYERS
DROPOUT	(32, 250)	$p = 0.25$
GRU	(64, 250)	INPUT SIZE 32, HIDDEN SIZE 64, 2 LAYERS
DROPOUT	(64, 250)	$p = 0.25$
RESHAPE	(10, 1600)	-
LINEAR	(10, 5)	INPUT FEATURES 1600, OUTPUT FEATURES 5

Table 8: Training Configuration for CNN+LSTM

PARAMETER	BATCH	OPTIMIZER	LEARNING RATE	SPLIT (TRAIN:VAL:TEST)	EARLY STOP
RAW EEG	64	ADAM	10^{-4}	7 : 1 : 2	PATIENCE 20 ON KAPPA
FREQUENCY-DOMAIN	256	ADAM	10^{-4}	7 : 1 : 2	PATIENCE 20 ON KAPPA
MICROSTATES	512	ADAM	10^{-4}	7 : 1 : 2	PATIENCE 20 ON KAPPA

Table 9: Sleep Transformer for Raw EEG

LAYER	OUTPUT	CONFIGURATION
-	(b , 6, 30000)	-
CONV1D	(b , 6, 6000)	INPUT CHANNELS 6, OUTPUT CHANNELS 6, KERNEL SIZE 5 STRIDE 5
CONV1D	(b , 6, 3000)	INPUT CHANNELS 6, OUTPUT CHANNELS 6, KERNEL SIZE 2 STRIDE 2
TRANSPOSE	(b , 3000, 6)	-
RESHAPE	($10b$, 300, 6)	-
RoFORMER	($10b$, 300, 256)	HIDDEN SIZE 256, 2 HIDDEN LAYERS, 4 HEADS, INTERMEDIATE SIZE 1024
SLICE AND RESHAPE	(b , 10, 256)	RETRIEVE ONLY THE FIRST ALONG THE SECOND DIMENSION AND RESHAPE
RoFORMER	(b , 10, 256)	HIDDEN SIZE 256, 2 HIDDEN LAYERS, 4 HEADS, INTERMEDIATE SIZE 1024
LINEAR	(b , 10, 5)	INPUT FEATURES 256, OUTPUT FEATURES 5

B.4.2 Training Configuration. This section lists the training configurations of the above three models. The models are trained on an NVIDIA-H20 GPU. The parameters in each case are optimized for performance and memory utilization.

B.5 ResNet Model for Motor Imagery Classification

Finally, we list our model for motor imagery classification.

B.5.1 Model Details.

Overview of model structure. The following shows the structure of ResNet model. Parameters are 20.3M, 21.5M and 21.4M. Model details are shown in Table 20, Table 21 and Table 22.

ELU. The ELU activation function is defined as

$$ELU(x) = \begin{cases} x & x > 0 \\ \alpha(e^x - 1) & x \leq 0 \end{cases}$$

Table 10: Sleep Transformer for Frequency-Domain

LAYER	OUTPUT	CONFIGURATION
–	$(b, 6, 1800)$	–
TRANSPOSE	$(b, 1800, 6)$	–
RESHAPE	$(10b, 180, 6)$	–
RoFORMER	$(10b, 180, 256)$	HIDDEN SIZE 256, 2 HIDDEN LAYERS, 4 HEADS, INTERMEDIATE SIZE 1024
SLICE AND RESHAPE	$(b, 10, 256)$	RETRIEVE ONLY THE FIRST ALONG THE SECOND DIMENSION AND RESHAPE
RoFORMER	$(b, 10, 256)$	HIDDEN SIZE 256, 2 HIDDEN LAYERS, 4 HEADS, INTERMEDIATE SIZE 1024
LINEAR	$(b, 10, 5)$	INPUT FEATURES 256, OUTPUT FEATURES 5

Table 11: Sleep Transformer for Microstates

LAYER	OUTPUT	CONFIGURATION
–	$(b, 30000)$	–
EMBEDDING	$(b, 30000, 128)$	NUMBER OF EMBEDDINGS 1002, DIMENSION 128
TRANSPOSE	$(b, 128, 30000)$	–
CONV1D	$(b, 128, 6000)$	INPUT CHANNELS 128, OUTPUT CHANNELS 128, KERNEL SIZE 5 STRIDE 5
CONV1D	$(b, 128, 3000)$	INPUT CHANNELS 128, OUTPUT CHANNELS 128, KERNEL SIZE 2 STRIDE 2
TRANSPOSE	$(b, 3000, 128)$	–
RESHAPE	$(10b, 300, 128)$	–
RoFORMER	$(10b, 300, 256)$	HIDDEN SIZE 256, 2 HIDDEN LAYERS, 4 HEADS, INTERMEDIATE SIZE 1024
SLICE AND RESHAPE	$(b, 10, 256)$	RETRIEVE ONLY THE FIRST ALONG THE SECOND DIMENSION AND RESHAPE
RoFORMER	$(b, 10, 256)$	HIDDEN SIZE 256, 2 HIDDEN LAYERS, 4 HEADS, INTERMEDIATE SIZE 1024
LINEAR	$(b, 10, 5)$	INPUT FEATURES 256, OUTPUT FEATURES 5

Table 12: Training Configuration for Sleep Transformer

PARAMETER	BATCH	OPTIMIZER	LEARNING RATE	SPLIT (TRAIN:VAL:TEST)	EARLY STOP
RAW EEG	64	ADAM	10^{-4}	7 : 1 : 2	PATIENCE 20 ON KAPPA
FREQUENCY-DOMAIN	1000	ADAM	10^{-4}	7 : 1 : 2	PATIENCE 20 ON KAPPA
MICROSTATES	512	ADAM	10^{-4}	7 : 1 : 2	PATIENCE 20 ON KAPPA

Table 13: ResNetFeatureExtractor

LAYER	OUTPUT	CONFIGURATION
–	$(6, 30000)$	–
CONV1D	$(64, 30000)$	INPUT CHANNELS 6, OUTPUT CHANNELS 64, KERNEL SIZE 7 PADDING 3
BATCHNORM1D	$(64, 30000)$	64
ReLU	$(64, 30000)$	–
MAXPOOL1D	$(64, 15000)$	KERNEL SIZE 3 STRIDE 2 PADDING 1
RESBLOCKS	$(512, 3000)$	RESBLOCKS(IN=64,OUT=512,STRIDE=5), SEE ABOVE
RESBLOCKS	$(128, 3000)$	RESBLOCKS(IN=512,OUT=128,STRIDE=1), SEE ABOVE
RESBLOCKS	$(256, 3000)$	RESBLOCKS(IN=128,OUT=256,STRIDE=1), SEE ABOVE
RESBLOCKS	$(512, 3000)$	RESBLOCKS(IN=256,OUT=512,STRIDE=1), SEE ABOVE

Embedding layer. For microstates, an embedding layer with vocabulary 1000 and dimension 1024 is employed. Convolution layers are used in the place of embedding for the other two representations.

B.5.2 Training Configuration. This section lists the training configurations of the above 3 models. The models are trained on an NVIDIA-H20 GPU. Model parameters in each case are optimized for performance and memory utilization.

Table 14: Sleep Net Zero for Raw EEG

LAYER	OUTPUT	CONFIGURATION
–	(6, 30000)	–
RESNETFEATUREEXTRACTOR	(512, 3000)	SEE ABOVE
TRANSPOSE	(3000, 512)	–
ROFORMER	(3000, 512)	HIDDEN SIZE 512, 2 HIDDEN LAYERS, 2 HEADS, INTERMEDIATE SIZE 1024
LINEAR	(3000, 5)	INPUT FEATURES 512, OUTPUT FEATURES 5
RESHAPE AND MEAN	(10, 5)	COMPUTE THE MEAN OF EVERY CONSECUTIVE 300 SCORES

Table 15: Sleep Net Zero for Frequency-Domain

LAYER	OUTPUT	CONFIGURATION
–	(6, 1800)	–
CONV1D	(640, 1800)	INPUT CHANNELS 6, OUTPUT CHANNELS 640, KERNEL SIZE 5 PADDING 2
CONV1D	(640, 360)	INPUT CHANNELS 640, OUTPUT CHANNELS 640, KERNEL SIZE 5 PADDING 5
CONV1D	(320, 360)	INPUT CHANNELS 640, OUTPUT CHANNELS 320, KERNEL SIZE 3 PADDING 1
CONV1D	(320, 180)	INPUT CHANNELS 320, OUTPUT CHANNELS 320, KERNEL SIZE 2 PADDING 2
CONV1D	(160, 180)	INPUT CHANNELS 320, OUTPUT CHANNELS 160, KERNEL SIZE 3 PADDING 1
TRANSPOSE	(180, 160)	–
ROFORMER	(180, 160)	HIDDEN SIZE 160, 2 HIDDEN LAYERS, 2 HEADS, INTERMEDIATE SIZE 1024
LINEAR	(180, 5)	INPUT FEATURES 160, OUTPUT FEATURES 5
RESHAPE AND MEAN	(10, 5)	COMPUTE THE MEAN OF EVERY CONSECUTIVE 18 SCORES

Table 16: Sleep Net Zero for Microstates

LAYER	OUTPUT	CONFIGURATION
–	(30000,)	–
EMBEDDING	(30000, 512)	NUMBER OF EMBEDDINGS 1002, DIMENSION 512
TRANSPOSE	(512, 30000)	–
CONV1D	(512, 6000)	INPUT CHANNELS 512, OUTPUT CHANNELS 512, KERNEL SIZE 5 PADDING 5
CONV1D	(256, 6000)	INPUT CHANNELS 512, OUTPUT CHANNELS 256, KERNEL SIZE 3 PADDING 1
CONV1D	(256, 3000)	INPUT CHANNELS 256, OUTPUT CHANNELS 256, KERNEL SIZE 2 PADDING 2
CONV1D	(128, 3000)	INPUT CHANNELS 256, OUTPUT CHANNELS 128, KERNEL SIZE 3 PADDING 1
TRANSPOSE	(3000, 128)	–
ROFORMER	(3000, 128)	HIDDEN SIZE 128, 2 HIDDEN LAYERS, 2 HEADS, INTERMEDIATE SIZE 1024
LINEAR	(3000, 5)	INPUT FEATURES 128, OUTPUT FEATURES 5
RESHAPE AND MEAN	(10, 5)	COMPUTE THE MEAN OF EVERY CONSECUTIVE 300 SCORES

Table 17: Training Configuration for Sleep Net Zero

PARAMETER	BATCH	OPTIMIZER	LEARNING RATE	SPLIT (TRAIN:VAL:TEST)	EARLY STOP
RAW EEG	96	ADAM	10^{-4}	7 : 1 : 2	PATIENCE 20 ON KAPPA
FREQUENCY-DOMAIN	512	ADAM	10^{-4}	7 : 1 : 2	PATIENCE 20 ON KAPPA
MICROSTATES	128	ADAM	10^{-4}	7 : 1 : 2	PATIENCE 20 ON KAPPA

C More Microstate Analysis

This section provides more analysis and visualization of microstates.

C.1 Comparison Between Wake Stage and Rapid Eye Movement (REM) Stage

Humans undergo vivid dreaming processes during REM stage [66]. In turn, EEG signals in REM stage share the same characteristics

Table 18: CNN for Raw EEG

LAYER	OUTPUT	CONFIGURATION
–	(6, 53000)	–
CONV1D	(1024, 53000)	INPUT CHANNELS 6, OUTPUT CHANNELS 1024, KERNEL SIZE 1
CONV1D AND RELU	(256, 10600)	INPUT CHANNELS 1024, OUTPUT CHANNELS 256, KERNEL SIZE 5 STRIDE 5
CONV1D AND RELU	(128, 2120)	INPUT CHANNELS 256, OUTPUT CHANNELS 128, KERNEL SIZE 5 STRIDE 5
CONV1D AND RELU	(128, 1060)	INPUT CHANNELS 128, OUTPUT CHANNELS 128, KERNEL SIZE 2 STRIDE 2
MAXPOOL1D	(128, 530)	KERNEL SIZE 2 STRIDE 2
DROPOUT	(128, 530)	$p = 0.1$
CONV1D AND RELU	(128, 530)	INPUT CHANNELS 128, OUTPUT CHANNELS 128, KERNEL SIZE 3 PADDING 1
CONV1D AND RELU	(128, 530)	INPUT CHANNELS 128, OUTPUT CHANNELS 128, KERNEL SIZE 3 PADDING 1
MAXPOOL1D	(128, 265)	KERNEL SIZE 2 STRIDE 2
DROPOUT	(128, 265)	$p = 0.1$
FLATTEN	(33920,)	–
LINEAR	(512,)	INPUT FEATURES 33920, OUTPUT FEATURES 512
DROPOUT	(512,)	$p = 0.1$
LINEAR	(256,)	INPUT FEATURES 512, OUTPUT FEATURES 256
DROPOUT	(256,)	$p = 0.1$
LINEAR	(64,)	INPUT FEATURES 256, OUTPUT FEATURES 64
DROPOUT	(64,)	$p = 0.1$
LINEAR	(3,)	INPUT FEATURES 64, OUTPUT FEATURES 3

Table 19: CNN for Frequency-Domain

LAYER	OUTPUT	CONFIGURATION
–	(6, 1590)	–
RESHAPE	(6, 265, 6)	LET THE LAST DIMENSION BE THE FREQUENCY BANDS
CONV2D	(1024, 265, 6)	INPUT CHANNELS 6, OUTPUT CHANNELS 1024, KERNEL SIZE (1, 1)
CONV2D & RELU	(256, 265, 6)	INPUT CHANNELS 1024, OUTPUT CHANNELS 256, KERNEL SIZE (1, 5) PADDING (0, 2)
CONV2D & RELU	(128, 265, 6)	INPUT CHANNELS 256, OUTPUT CHANNELS 128, KERNEL SIZE (1, 5) STRIDE (0, 2)
CONV2D & RELU	(128, 265, 6)	INPUT CHANNELS 128, OUTPUT CHANNELS 128, KERNEL SIZE (1, 3) STRIDE (0, 1)
MAXPOOL2D	(128, 265, 3)	KERNEL SIZE (1, 2) STRIDE (1, 2)
DROPOUT	(128, 265, 3)	$p = 0.1$
CONV2D & RELU	(128, 265, 3)	INPUT CHANNELS 128, OUTPUT CHANNELS 128, KERNEL SIZE (1, 3) PADDING (0, 1)
CONV2D & RELU	(128, 265, 3)	INPUT CHANNELS 128, OUTPUT CHANNELS 128, KERNEL SIZE (1, 3) PADDING (0, 1)
MAXPOOL2D	(128, 265, 1)	KERNEL SIZE (1, 2) STRIDE (1, 2)
DROPOUT	(128, 265, 1)	$p = 0.1$
FLATTEN	(33920,)	–
LINEAR	(512,)	INPUT FEATURES 33920, OUTPUT FEATURES 512
DROPOUT	(512,)	$p = 0.1$
LINEAR	(256,)	INPUT FEATURES 512, OUTPUT FEATURES 256
DROPOUT	(256,)	$p = 0.1$
LINEAR	(64,)	INPUT FEATURES 256, OUTPUT FEATURES 64
DROPOUT	(64,)	$p = 0.1$
LINEAR	(3,)	INPUT FEATURES 64, OUTPUT FEATURES 3

with that during wakefulness. We analyze the 30 most frequent-appearing microstates during W and REM stages across groups of 30 subjects. The results are as follows:

From the above tables we see that the 4 microstates 161, 385, 419 and 421 occur frequently in both R and W stages, with roughly the same ranks. This suggests that the brain undergoes similar activity patterns during these stages.

Further examination of these microstates shows that these microstates have low potential which is below $10\mu V$. This is consistent with the fact that during W stage, brain signals are dominated by α waves which have a low potential. Also, this result indicates certain similarities between W stage and R stage since the brain undergoes similar activity.

Table 20: CNN for Microstates

LAYER	OUTPUT	CONFIGURATION
–	(6, 53000)	–
EMBEDDING	(1024, 53000)	NUMBER OF EMBEDDINGS 1001, DIMENSION 1024
CONV1D AND RELU	(256, 10600)	INPUT CHANNELS 1024, OUTPUT CHANNELS 256, KERNEL SIZE 5 STRIDE 5
CONV1D AND RELU	(128, 2120)	INPUT CHANNELS 256, OUTPUT CHANNELS 128, KERNEL SIZE 5 STRIDE 5
CONV1D AND RELU	(128, 1060)	INPUT CHANNELS 128, OUTPUT CHANNELS 128, KERNEL SIZE 2 STRIDE 2
MAXPOOL1D	(128, 530)	KERNEL SIZE 2 STRIDE 2
DROPOUT	(128, 530)	$p = 0.1$
CONV1D AND RELU	(128, 530)	INPUT CHANNELS 128, OUTPUT CHANNELS 128, KERNEL SIZE 3 PADDING 1
CONV1D AND RELU	(128, 530)	INPUT CHANNELS 128, OUTPUT CHANNELS 128, KERNEL SIZE 3 PADDING 1
MAXPOOL1D	(128, 265)	KERNEL SIZE 2 STRIDE 2
DROPOUT	(128, 265)	$p = 0.1$
FLATTEN	(33920,)	–
LINEAR	(512,)	INPUT FEATURES 33920, OUTPUT FEATURES 512
DROPOUT	(512,)	$p = 0.1$
LINEAR	(256,)	INPUT FEATURES 512, OUTPUT FEATURES 256
DROPOUT	(256,)	$p = 0.1$
LINEAR	(64,)	INPUT FEATURES 256, OUTPUT FEATURES 64
DROPOUT	(64,)	$p = 0.1$
LINEAR	(3,)	INPUT FEATURES 64, OUTPUT FEATURES 3

Table 21: Training Configuration for CNN

PARAMETER	BATCH	OPTIMIZER	LEARNING RATE	SPLIT (TRAIN:VAL:TEST)	EARLY STOP
RAW EEG	128	ADAM	5×10^{-4}	7 : 1 : 2	PATIENCE 100 ON KAPPA
FREQUENCY-DOMAIN	128	ADAM	5×10^{-4}	7 : 1 : 2	PATIENCE 100 ON KAPPA
MICROSTATES	128	ADAM	10^{-4}	7 : 1 : 2	PATIENCE 100 ON KAPPA

Table 22: ResNet for Raw EEG

LAYER	OUTPUT	CONFIGURATION
–	(6, 640)	–
CONV1D	(1024, 640)	INPUT CHANNELS 6, OUTPUT CHANNELS 1024, KERNEL SIZE 3 PADDING 1
ENCODER	(128, 640)	SEE BELOW
FLATTEN	(81920,)	–
CLASSIFIER	(4,)	SEE BELOW

Table 23: ResNet for Frequency-Domain

LAYER	OUTPUT	CONFIGURATION
–	(6, 24)	–
CONV1D	(1024, 24)	INPUT CHANNELS 6, OUTPUT CHANNELS 1024, KERNEL SIZE 3, PADDING 1
ENCODER 2	(256, 24)	SEE BELOW
FLATTEN	(6144,)	–
CLASSIFIER 2	(4,)	SEE BELOW

Table 24: ResNet for Microstates

LAYER	OUTPUT	CONFIGURATION
–	(6, 640)	–
CONV1D	(1024, 640)	INPUT CHANNELS 6, OUTPUT CHANNELS 1024, KERNEL SIZE 3, PADDING 1
ENCODER	(128, 640)	SEE BELOW
FLATTEN	(81920,)	–
CLASSIFIER	(4,)	SEE BELOW

Table 25: Encoder Architecture

LAYER	OUTPUT	CONFIGURATION
–	(1024, 640)	–
CONV1D	(512, 640)	INPUT CHANNELS 1024, OUTPUT CHANNELS 512, KERNEL SIZE 13, PADDING 6
RESBLOCK1D	(256, 640)	IN 512, OUT 256, KERNEL 11, SEE BELOW
RESBLOCK1D	(128, 640)	IN 256, OUT 128, KERNEL 9, SEE BELOW
RESBLOCK1D	(128, 640)	IN 128, OUT 128, KERNEL 7, SEE BELOW
ELU	(128, 640)	–

Table 26: Encoder 2 Architecture

LAYER	OUTPUT	CONFIGURATION
–	(1024, 24)	–
CONV1D	(768, 24)	INPUT CHANNELS 1024, OUTPUT CHANNELS 768, KERNEL SIZE 13, PADDING 6
RESBLOCK1D	(512, 24)	IN 768, OUT 512, KERNEL 11, SEE BELOW
RESBLOCK1D	(256, 24)	IN 512, OUT 256, KERNEL 9, SEE BELOW
RESBLOCK1D	(256, 24)	IN 256, OUT 256, KERNEL 7, SEE BELOW
ELU	(256, 24)	–

Table 27: Classifier Architecture

LAYER	OUTPUT	CONFIGURATION
–	(81920,)	–
LINEAR AND RELU	(128,)	IN FEATURES 81920, OUT FEATURES 128
LINEAR AND RELU	(128,)	IN FEATURES 128, OUT FEATURES 128
LINEAR AND RELU	(64,)	IN FEATURES 128, OUT FEATURES 64
LINEAR	(4,)	IN FEATURES 64, OUT FEATURES 4

Table 28: Classifier 2 Architecture

LAYER	OUTPUT	CONFIGURATION
–	(6144,)	–
LINEAR AND RELU	(128,)	IN FEATURES 6144, OUT FEATURES 128
LINEAR AND RELU	(128,)	IN FEATURES 128, OUT FEATURES 128
LINEAR AND RELU	(64,)	IN FEATURES 128, OUT FEATURES 64
LINEAR	(4,)	IN FEATURES 64, OUT FEATURES 4

Table 29: Training Configuration for ResNet

PARAMETER	BATCH	OPTIMIZER	LEARNING RATE	SPLIT (TRAIN:VAL:TEST)	EARLY STOP
RAW EEG	128	ADAM	5×10^{-4}	7 : 1 : 2	PATIENCE 100 ON KAPPA
FREQUENCY-DOMAIN	128	ADAM	5×10^{-4}	7 : 1 : 2	PATIENCE 100 ON KAPPA
MICROSTATES	128	ADAM	2×10^{-6}	7 : 1 : 2	PATIENCE 10 ON KAPPA

Table 30: Rank among Subjects under W Stage

MICROSTATE	RANK AMONG 10 GROUPS OF SUBJECTS									
⋮	⋮									
160	24	29	23	23	30	25	26	25	20	27
161	14	11	16	17	14	15	15	14	19	14
162	917	827	892	872	814	775	839	813	807	858
⋮	⋮									
384	229	166	236	165	188	218	150	220	258	165
385	3	2	3	2	4	2	3	2	3	2
386	338	721	589	677	543	640	654	531	402	634
⋮	⋮									
418	701	519	470	667	672	659	597	511	409	587
419	1	1	1	1	1	1	1	1	1	1
420	537	396	645	619	592	608	670	609	607	654
421	2	3	2	3	2	3	2	3	2	3
422	573	434	515	458	496	508	525	494	349	548
⋮	⋮									

Table 31: Rank among Subjects under R Stage

MICROSTATE	RANK AMONG 10 GROUPS OF SUBJECTS									
⋮	⋮									
160	27	23	24	22	26	23	25	25	20	24
161	15	15	18	21	14	14	21	16	22	21
162	831	810	840	699	672	762	772	688	882	720
⋮	⋮									
384	158	156	202	202	168	180	174	192	220	200
385	5	4	7	3	4	3	8	3	3	3
386	544	626	712	818	818	817	773	736	714	634
⋮	⋮									
418	466	639	569	527	634	592	557	594	528	616
419	1	1	2	1	1	1	1	1	1	1
420	589	671	731	581	631	711	753	644	811	722
421	3	2	1	2	2	2	2	2	2	2
422	420	386	368	281	460	332	381	352	325	346
⋮	⋮									

C.2 Comparison Between the Wake Stage and the Non-Rapid Eye Movement III Stage

NREM3 stage denotes deep sleep. In this case, the brain activity differs from that in the wake stage.

Table 32: Rank among Subjects under N3 Stage

MICROSTATE	RANK AMONG 10 GROUPS OF SUBJECTS									
⋮	⋮									
377	625	396	672	703	134	737	748	577	358	771
378	1	2	3	1	2	2	1	2	2	1
379	800	888	799	845	825	832	830	824	817	791
⋮	⋮									
451	753	811	707	779	627	755	822	871	614	782
452	18	7	10	10	10	15	8	5	13	8
453	939	979	915	881	902	932	709	910	965	899
⋮	⋮									
650	28	148	89	244	117	68	109	170	135	120
651	6	4	13	2	4	6	3	4	3	2
652	913	908	793	786	929	814	850	755	872	784
⋮	⋮									

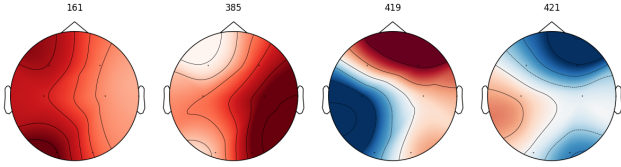


Figure 10: Visualizing Microstates 161, 385, 419 and 421

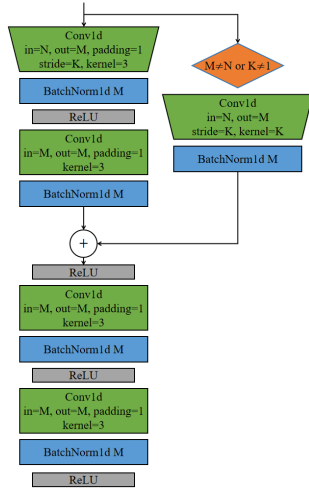


Figure 8: The Model Structure of ResBlocks with $in=N$, $out=M$ and $stride=K$

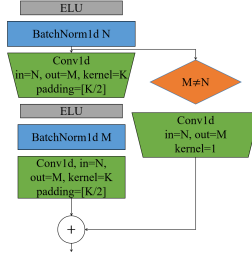


Figure 9: The Model Structure of ResBlock1d with $in=N$, $out=M$ and $kernel=K$

From the microstates distribution we see that the dominant microstates are different from that of W stage. To further back this observation, we record the rank of microstates 378, 452, 385 across W and N3 stage.

Results demonstrate that the microstates that frequently occur during W stage typically occur rarely in N3 stage. This again shows that the brain activity differs considerably between these 2 stages.

We further visualize the microstates:

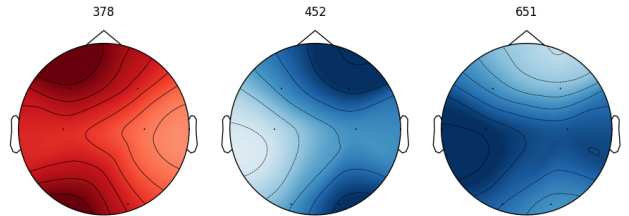


Figure 11: Visualizing Microstates 378, 452 and 651

and we see that these microstates correspond to a state with a relatively high potential, typically $> 10\mu V$. This is consistent with the fact that during N3 stage, brain activity is dominated by δ waves which has a high amplitude [77]. Nonetheless, EEG signals are oscillating and will not always remain at a high voltage, hence in certain states like the microstates dominating in W stage will also occur with a relatively high frequency.

Table 33: Rank among Subjects under N3 Stage

MICROSTATE		RANK AMONG 10 GROUPS OF SUBJECTS									
378	W	132	120	214	146	169	158	109	165	172	163
	N3	0	1	2	0	1	1	0	1	1	0
452	W	95	85	166	98	112	115	112	100	143	132
	N3	17	6	9	9	9	14	7	4	12	7
421	W	3	2	1	2	2	2	2	2	2	2
	N3	489	124	26	52	278	161	71	54	34	78

microstate	rank	microstate	rank	microstate	rank
378	1	⋮	⋮	⋮	⋮
⋮	⋮	378	2	487	2
651	6	⋮	⋮	378	3
⋮	⋮	⋮	⋮	⋮	⋮
487	14	651	4	⋮	⋮
⋮	⋮	⋮	⋮	452	10
452	18	452	7	⋮	⋮
⋮	⋮	⋮	⋮	651	13
⋮	⋮	⋮	⋮	⋮	⋮
⋮	⋮	487	11	⋮	⋮
⋮	⋮	⋮	⋮	⋮	⋮
⋮	⋮	⋮	⋮	⋮	⋮

subjects 1 ~ 30 N3 stage subjects 31 ~ 60 N3 stage subjects 61 ~ 90 N3 stage

Table 36: Rank among Subjects under N3 Stage

microstate	rank	microstate	rank	microstate	rank
419	1	419	1	419	1
421	2	385	2	421	2
385	3	421	3	385	3
⋮	⋮	⋮	⋮	⋮	⋮
⋮	⋮	⋮	⋮	⋮	⋮
333	7	333	6	333	7
⋮	⋮	⋮	⋮	⋮	⋮
⋮	⋮	⋮	⋮	⋮	⋮
161	14	161	11	161	16
⋮	⋮	⋮	⋮	⋮	⋮
⋮	⋮	⋮	⋮	⋮	⋮
⋮	⋮	⋮	⋮	⋮	⋮

subjects 1 ~ 30 W stage subjects 31 ~ 60 W stage subjects 61 ~ 90 W stage

Table 35: Rank among Subjects under N3 Stage

microstate	rank	microstate	rank	microstate	rank
419	1	419	1	421	1
333	2	421	2	419	2
421	3	333	3	333	3
⋮	⋮	385	4	⋮	⋮
⋮	⋮	⋮	⋮	⋮	⋮
385	5	⋮	⋮	385	7
⋮	⋮	⋮	⋮	⋮	⋮
⋮	⋮	⋮	⋮	⋮	⋮
161	15	161	11	161	18
⋮	⋮	⋮	⋮	⋮	⋮
⋮	⋮	⋮	⋮	⋮	⋮
⋮	⋮	⋮	⋮	⋮	⋮

subjects 1 ~ 30 R stage subjects 31 ~ 60 R stage subjects 61 ~ 90 R stage

Table 34: Rank among Subjects under N3 Stage

C.3 Comparing other Sleep Stages

For sleep stage N1 and N2, the dominant microstates are also 419, 385, 421, 615 and other states found in W stage. This suggests that these microstates capture a class of weak EEG signals that the brain usually switches between. Also, the brain activity in stages N1 and N2 shares certain aspects with that in W stage.

We also found that when transforming from stage W through stage N1, stage N2 and finally to stage N3, the frequency of microstate 489 is increasing. The visualization of 489 is as follows:

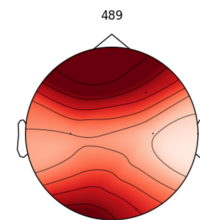


Figure 12: Visualizing Microstates 489

which also has relatively high potential with all leads between 2 ~ 14 μ V. This again shows that from W through N1, N2 to N3, high amplitude brain activity becomes more and more common.